

# Statistical Models of Rough Surfaces for Finite Element 3D-Contact Analysis

Ryszard Buczkowski · Michal Kleiber

Received: 22 June 2009 / Accepted: 22 June 2009 / Published online: 23 September 2009  
© CIMNE, Barcelona, Spain 2009

**Abstract** The present study is divided in two parts. In the first one the complete elasto-plastic microcontact model of anisotropic rough surfaces is given. Rough surfaces are modelled as a random process in which the height of the surface is considered to be a two-dimensional random variable. It is assumed that the surface is statistically homogeneous. The description of anisotropic random surfaces is concentrated on strongly rough surfaces; for such surfaces the summits are represented by highly eccentric elliptic paraboloids. The model is based on the volume conservation of asperities with the plasticity index modified to suit more general geometric contact shapes during plastic deformation process. This model is utilized to determine the total contact area, contact load and contact stiffness which are a combination of the elastic, elasto-plastic and plastic components. The elastic and elasto-plastic stiffness coefficients decrease with increasing variance of the surface height about the mean plane. The standard deviation of slopes and standard deviation of curvatures have no observable effects on the normal contact stiffness. The part two deals with the solution of the fully three-dimensional contact/friction problem taking into account contact stiffnesses in the normal and tangential directions. An incremental non-associated hardening friction law model analogous to the classical theory of plasticity is used. Two numerical examples are selected to show applicability of the method proposed.

## 1 Introduction

Modelling of the contact of rough surfaces has been treated using a number of approaches. The classical statistical model for a combination of the elastic and plastic contact between rough surfaces model of Greenwood and Williamson [1] (GW model) has been widely accepted. It assumes that asperities are modelled by a set of spheres of constant radius equivalent to an average curvature of the asperities and the deformation of any point in the roughness layer is independent of its neighbouring points. The last assumption, however, cannot be accepted for higher contact normal loads. On the basis of the finite element results according to Komvopoulos and Choi [2] interaction effects of neighboring asperities strongly depend on the distribution and radius of asperities and indentation depth. They concluded that the effect of neighboring asperities manifests itself through the unloading and superposition mechanisms. A surface of GW model can be characterized by two following parameters: the standard deviation of surface heights  $\sigma$  or  $R_q$  which is referred to the square root of  $m_0$  and the area density of peaks and summits. Greenwood and Williamson [1] introduced the idea of studying three-point peaks. They defined the peak as a sample point on the profile which is higher than their immediate neighbours at the sampling interval, while the summit as a point on the two-dimensional surface higher than all its neighbours. In this case the summit of roughness is defined in the majority of cases as a point for which eight neighbouring points are situated below. The GW model assumes that summits on surface are equivalent to peaks on profiles. Clearly it is not true, the summit density can be estimated from the peak density squared, but the factor is not 1 as assumed by Greenwood and Williamson [1]. According to the five-point summits theory of Greenwood from 1984 [3], the discrepancy between the density of summits

---

R. Buczkowski (✉)  
Maritime University of Szczecin, Division of Computer Methods,  
H. Pobożnego 11, 70-507 Szczecin, Poland  
e-mail: rbuczkowski@ps.pl

M. Kleiber  
Institute of Fundamental Technological Research, Polish  
Academy of Sciences, Pawinskiego 5B, 02-106 Warsaw, Poland

and peaks increases when the sampling interval is larger and rises to the asymptotic value of 1.8. For complete description of the isotropic GW model we need also the information about the distance between the summit mean plane and the surface mean plane which depends on the bandwidth parameter  $\alpha$ , defined as

$$\alpha = \frac{m_0 m_4}{m_2^2},$$

where  $m_0$ ,  $m_2$  and  $m_4$  are the zeroth, second and fourth spectral moments of the profile. In the limit as the sampling interval tends to zero the moments of the power spectrum  $m_0$ ,  $m_2$  and  $m_4$  become equal to the quantities  $\sigma^2$ ,  $\sigma_m^2$  and  $\sigma_\kappa^2$  which are the mean square values of the height, slope and curvature, respectively, (see Greenwood [3]).

Another of the methods is a fractal description of engineering surfaces being presently a subject of the intensive discussion. Because the conventional parameters like slopes and curvatures are very scale-sensitive, attractiveness of the fractal model consists in its ability to predict the relationship between roughness parameters and sampling size or the resolution of the measuring instrument. The surface roughness can be adequately described using self-affine fractal models. A self-affine fractal object needs to be characterized by at least two parameters defined as the fractal dimension  $D$  which describes how roughness changes with scale and the amplitude parameter (sometimes called topothesy)  $\Lambda$  defined as the horizontal separation of pairs of points on a surface corresponding to an average slope of one radian. A number of methods have been suggested in the literature to estimate both the  $D$  and  $\Lambda$  parameters. The structure function, spectral, the variogram, roughness-length and line scaling methods were used to calculate fractal parameters. Many authors showed that the fractal parameters are scale dependent, which arise from the sampling size, sampling interval and the resolution of the scanning instrument. Fardin *et al.* [4, 5] used a 3D laser scanner having high accuracy and resolution to investigate the scale dependent behaviour of a large and rough rock fracture. Four sampling windows were selected from the central part of the modified digital replica. Their results show that both  $D$  and  $\Lambda$  are scale dependent and their values decrease with increasing size of the sampling windows of the 3D-laser scanner. The authors obtained a power law relation between the standard deviations of the reduced asperity height and the window sizes for the all sampling windows. They concluded that the scale-dependency is always limited to a certain size, defined as the stationarity threshold, below which reliable statistical properties of the joint surface cannot be extracted. Moreover, rougher surfaces will have a larger stationarity limit and therefore, for accurate characterization of the rock fracture surface roughness, samples with a size larger than or equal to stationarity limit are necessary. In the note of Whitehouse [6] the author

questions the philosophy of using fractals to describe engineering surfaces. Greenwood [7] in his comments on the paper of Whitehouse also doubts about the fractal concept.

In the case of statistical methods the question that now remains to be answered is whether the profile parameters vary with the sampling size or the instrument resolution. Both the theory and experiment show that the density of peaks or summits and curvatures do all depend on the sampling interval. When the sampling interval is reduced by the factor of 10, the summit density increases by a factor of 40. Much the same holds for curvatures [3]. Additionally, in the recent work of Greenwood and Wu [8], the authors stated that their idea based on assumption that peaks on a surface profile (points higher than their immediate neighbours at the sampling interval used) is quite wrong and gives false results according to both the number and the radius of curvature of the asperities. A similar problem occurs in the 3D description of surface. Radziejewska [9] have recently proposed entirely new method of surface roughness modelling with one effective radius which is much larger than the one obtained from measurements. The proposed method is based on the 3D analysis of size and shape of the surface intersection asperities with planes parallel to the mean plane. It provides much more information than the standard bearing curve, which additionally enables to define the contact process in the beginning phase of the approach.

Fortunately, the experimental data for the thin-film disks and magnetic tapes clearly show that the r.m.s. of  $m_0$  referred to  $\sigma$  or  $R_q$  does not change [10] or varies very little for machined surfaces with sampling interval [11] and can therefore be considered as scale independent for most surfaces and used to characterize a rough surface uniquely. The last conclusion fits very well to the present formulation because the standard deviation of slopes and curvatures have no observable effects on the elastic or elasto-plastic normal stiffness while both the elastic and elasto-plastic stiffness coefficients depend primarily on the variance of the surface height about the mean plane  $m_{00}$  (after Sayles and Thomas [12] and McColl [13],  $m_{00} = m_0$ ), which is not much sensitive over a large range of sampling intervals. Additionally,  $R_q = \sqrt{m_0}$  is the most useful and recognized parameter in the surface metrology thus being embedded in the international standards.

For machined metal surfaces the height, slope and curvature of asperities are random and have the Gaussian or nearly Gaussian probability distribution. This fact suggests that the geometry of such surfaces can be described statistically assuming they are described by a limited number of variables. On the basis of probability theory Whitehouse and Archard [14], Nayak [15, 16], Bush, Gibson and Thomas [17] and Bush, Gibson and Keogh [18, 19], Sayles and Thomas [20], Whitehouse and Phillips [21–23] have made an important advancement in developing the asperity based-model.

The observation of Pullen and Williamson [24] that the volume of deformed asperities is conserved stimulated Chang, Etsion and Bogy [25] (CEB model) to adopt it in their elasto-plastic model of deformed spheres. They introduced an improved model where the asperity deformations are primarily elastic but there is also a significant number of asperities beyond their elastic limit. Recently, Horng [26] extended the CEB model to describe a more general case of an elliptical contact of asperities. On the other hand, surfaces machined by turning, honing or grinding, have orientation corresponding to the direction of motion of the cutting tools relative to the workpieces, and a model of anisotropic rough surfaces must be then employed. In such cases, it is necessary to include both the principal curvatures taking into account the directional nature of surface roughness. To do so, the asperities may be replaced by elliptic paraboloid and then the analysis due to Hertz may be employed for elastic deformation of the surfaces. The statistical theory of Longuet-Higgins [27, 28] in its general form provides a complete description of random anisotropic surfaces. Nayak [16] considered the application of the Longuet-Higgins [27, 28] theory to anisotropic engineering surfaces and demonstrated how the spectrum moments up to order 4 can be obtained by knowing seven profile parameters (invariants) of the surface. These parameters, which are determinants of correlation matrices used in the multi-dimensional normal distribution theory are termed invariants of the surface and are independent of the orientation of the coordinate axes. Each of these invariants was discussed by Nayak [16] in terms of its respective physical interpretation. For a general analysis, five non-parallel profiles are required to calculate the surface moments  $m_{ij}$  in terms of the profile moments  $m_n(\theta)$ . A case of engineering importance is the surface with a grain pronounced to one direction. A theoretical analysis of such surfaces was presented by Bush and co-authors [17–19]. They derived a joint distribution density function for random asperity heights and curvatures of elliptic paraboloids in elastic contact with a smooth rigid flat for both the isotropic [17, 18] and anisotropic surface [19]. An interesting fact about nonisotropic surfaces is that one needs nine constants (spectral profile moments  $m_{ij}$ ) to proceed with the analysis of the surface statistics. However, the properties of the surface are independent of the orientation of the plane reference surface coordinates  $(x, y)$ . In relation to the anisotropic case Bush, Gibson and Keogh [19] simplified the general anisotropic rough surfaces to a strongly anisotropic one. In this case it is sufficient to consider five surface parameters: the variance of the surface height  $m_{00}$ , two principal mean square slopes  $m_{02}$ ,  $m_{20}$  and two principal mean square curvatures:  $m_{04}$ ,  $m_{40}$ . A more general description of anisotropic surfaces was recently presented by So and Liu [29]. This approach showed that the plastic part of the contact area increases significantly as the degree of anisotropy increases. McCool and Gassel [30] gave

the mathematical basis for anisotropic description using the Monte Carlo simulation technique. Another approach was taken by Kucharski *et al.* [31], Kogut and Etsion [32], Larson *et al.* [33], Faulkner and Arnell [34], Lin and Lin [35] (an elliptical microcontact), Yang and Komvopoulos [36], Hyun *et al.* [37] and Pei *et al.* [38] who proposed a finite element model to determine a more realistic elasto-plastic or elasto-viscoplastic deformation for the analysis of a single-asperity behaviour, and then the relations derived were combined with a statistical or factual description of the rough surface.

Different approaches have been considered to describe micromechanical contact laws. The available formulations are based either on curve-fitting of experimental results or on statistical analysis of rough surfaces. Comprehensive review of such models has been recently presented by Wriggers [39]. An extensive survey of statistical models of rough surfaces was made by Thomas [40], Bhushan [41–43], Whitehouse [44], Ciavarella *et al.* [45, 46] and Persson *et al.* [47]. Relations between surface parameters of the profilometric and various asperity-based models were summarized by McCool [48]. According to him, for the isotropic case the prediction of nominal pressure assuming the bandwidth parameter  $\alpha = 10$  is lower by nearly a factor of 2 in comparison to the elastic isotropic model taken from Reference of Bush, Gibson and Thomas [17] (BGT model) but is in good accordance with an asymptotic solution of the BGT model and the GW model. The question why the agreement is not better at higher bandwidth parameters  $\alpha$  is not known [48]. The suggestion of Mcool that it could be due to truncation errors in the numerical integrations is not justified. A comparison of all simplified models to the strongly anisotropic model of Bush, Gibson and Keogh [19] (BGK) is therein not given. It appears that the statistical roughness models given in the context to the finite element procedure by Willner and Gaul [49], Zavarise and Schrefler [50] (both related to the elastic case) and Buczkowski and Kleiber [51, 52] (the elasto-plastic case) were published first.

This study concentrates on building an elasto-plastic statistical model of rough surfaces for which the joint stiffness can be determined in a general way. In Sect. 2, we begin with a complete description of anisotropic random surfaces to be restricted here to strongly rough surfaces; for such surfaces the summits are represented by highly eccentric elliptic paraboloids having their semimajor axes oriented in the direction of the grain. The statistical description of random, strongly anisotropic Gaussian surfaces based on the model of Bush, Gibson and Keogh [19] is adopted. To calculate the forces and contact area for the single asperity in the elastic range the solution of Hertz is used (Sect. 3). Section 5 presents an elasto-plastic micromechanical model of rough surfaces which is based on volume conservation during fully plastic deformation. To analyse the elasto-plastic elliptic microcontact the idea of Zhao *et al.* [53] and Wang [54]

(the model considers the continuity and smoothness joining the expressions for elastic and fully plastic areas as functions of interference) was utilized (Sect. 6). Both the elastic and elasto-plastic normal contact coefficients are derived in Sects. 4 and 7, respectively. Section 8 deals with the solution of the fully three-dimensional contact/friction problem taking into account elasto-plastic contact stiffnesses of the surfaces. An incremental non-associated hardening friction law model is used. Section 9 is devoted to the finite element incremental solution of fully three-dimensional contact problem. Two numerical examples have been selected to show applicability of the method proposed. Some conclusions are presented in last section.

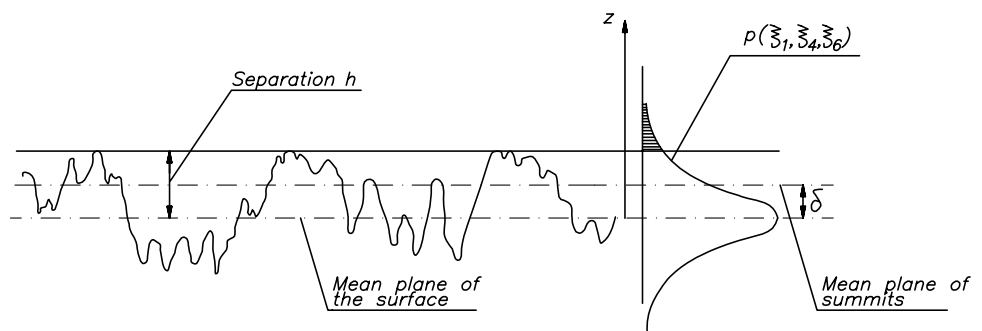
### 2 Strongly Anisotropic Model of Rough Surfaces

Theories of isotropic surfaces are not applicable to the important practical case of ground surfaces which are strongly anisotropic. Bush, Gibson and Keogh [19] presented the random theory of strongly anisotropic rough surfaces which will be briefly described here. Figure 1 presents a randomly rough surface in contact with a smooth flat. In the model the cap of each asperity is replaced by elliptic paraboloid with summit  $\xi_1$  above the point  $(x_0 = 0, y_0 = 0)$  on the mean plane (Fig. 2). The plane  $z = h$  intersects the paraboloid in an ellipse which has semi-axes of lengths (in a local deformed stage)  $A$  and  $B$  with one its principal radii of curvature at angle  $\beta = 0$  to the positive  $x$ -axis. Let us consider a rough surface whose heights above the mean plane of the surface are defined by  $z(x, y)$ , where  $x, y$  are the Cartesian coordinates in the mean plane of the surface in which the profile area within the sampling length above the surface is equal to that below it. Note that the mean plane of the surface is situated below the mean plane of the summits by an amount marked at the Fig. 1 by  $\delta$ .

Defining

$$\begin{aligned} \xi_1 = z, \quad \xi_2 = \frac{\partial z}{\partial x}, \quad \xi_3 = \frac{\partial z}{\partial y}, \\ \xi_4 = \frac{\partial^2 z}{\partial x^2}, \quad \xi_5 = \frac{\partial^2 z}{\partial x \partial y}, \quad \xi_6 = \frac{\partial^2 z}{\partial y^2}, \end{aligned} \tag{1}$$

**Fig. 1** Contact of a randomly rough surface with a smooth flat. The distance between the mean plane of the surface and the mean plane of the summits is denoted by  $\delta$



the joint probability density of the normally distributed variables  $\xi_i$  ( $i = 1, 2, \dots, 6$ ), each being the sum of a large number of independent variables with zero expectation, is

$$p(\xi_1, \xi_2, \dots, \xi_6) = \frac{1}{(2\pi)^3 \Delta^{1/2}} \exp\left(-\frac{1}{2} M_{ij} \xi_i \xi_j\right), \tag{2}$$

where  $M_{ij}$  is the inverse of the positive-defined covariance matrix  $N_{ij}$

$$N_{ij} = \begin{bmatrix} E[\xi_1^2] & E[\xi_1 \xi_2] & \dots & E[\xi_1 \xi_6] \\ E[\xi_2 \xi_1] & E[\xi_2^2] & \dots & E[\xi_2 \xi_6] \\ \vdots & \vdots & \vdots & \vdots \\ E[\xi_6 \xi_1] & E[\xi_6 \xi_2] & \dots & E[\xi_6^2] \end{bmatrix} \tag{3}$$

and  $\Delta$  is the determinant of  $N_{ij}$ . Considering the random variables with zero mean, the components of the matrix  $N_{ij}$  in (3) are the expectations of  $\xi_i \xi_j$  which can be written in following way

$$E[\xi_i \xi_j] = \overline{\xi_i \xi_j} = n_{ij}. \tag{4}$$

According to Longuet-Higgins [16] the spectral moments can be defined by the power spectral density (called there the energy spectrum)

$$m_{ij} = \int_{-\infty}^{\infty} \int_{-\infty}^{\infty} \Phi(u, v) u^i v^j du dv, \tag{5}$$

where  $\Phi(u, v)$  is the power spectral density and  $u$  and  $v$  are the wave numbers. (The power spectral density is the Fourier transform of the surface autocorrelation function.) The elements of the covariance matrix  $N_{ij}$  are computed in Appendix A.

Choosing the  $x$ -axis in the direction of the grain, symmetry implies that

$$m_{11} = m_{13} = m_{31} = 0. \tag{6}$$

Restricting the theory to the case of highly eccentric asperities with their axes closely aligned to the  $x$ -direction leads to  $m_{22}$  being negligible (see Bush *et al.* [19]). In this case it is

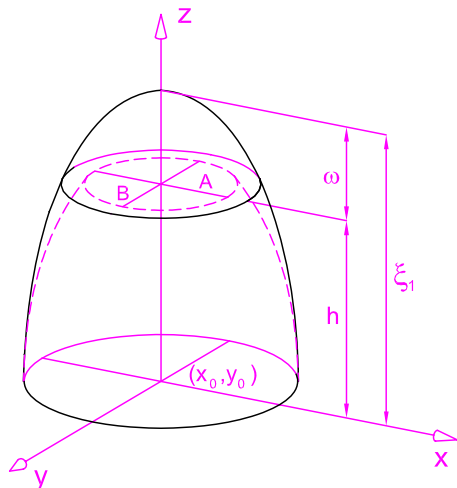


**Fig. 2** Geometry a single contacting asperity in form of elliptic paraboloid

sufficient to consider the probability density of the variables of  $\xi_1, \xi_2, \xi_3, \xi_4$  and  $\xi_6$ , so that (2) becomes now

$$p(\xi_1, \xi_2, \xi_3, \xi_4, \xi_6) = \frac{1}{(2\pi)^{5/2} \Delta^{1/2}} \exp\left(-\frac{1}{2} M_{ij} \xi_i \xi_j\right), \quad (7)$$

where  $M_{ij}$  is the inverse of the simplified matrix  $N_{ij}$  given as

$$N_{ij} = \begin{bmatrix} m_{00} & 0 & 0 & -m_{20} & -m_{02} \\ 0 & m_{20} & 0 & 0 & 0 \\ 0 & 0 & m_{02} & 0 & 0 \\ -m_{20} & 0 & 0 & m_{40} & 0 \\ -m_{02} & 0 & 0 & 0 & m_{04} \end{bmatrix}. \quad (8)$$

The determinant  $\Delta$  of  $N_{ij}$  is found to be

$$\Delta = m_{00} m_{40} m_{04} m_{20} m_{02} \mu, \quad (9)$$

where

$$\mu = (1 - \beta_1 - \beta_2) \quad (10)$$

while  $\beta_1$  and  $\beta_2$  are defined by the bandwidth parameters  $\alpha_1$  and  $\alpha_2$  in the  $x$ - and  $y$ -directions, respectively, as

$$\alpha_1 = \frac{1}{\beta_1} = \frac{m_{00} m_{40}}{m_{20}^2}, \quad \alpha_2 = \frac{1}{\beta_2} = \frac{m_{00} m_{04}}{m_{02}^2}. \quad (11)$$

For strongly anisotropic surfaces five parameters are required to describe such surfaces: (1)  $m_{00}$ , i.e. variance of the surface height about the mean plane, (2)  $m_{02}$  and  $m_{20}$ , i.e. the principal mean square slopes, (3)  $m_{04}$  and  $m_{40}$ , i.e. the principal mean square curvatures. According to Longuet-Higgins [28], Nayak [15], Sayles and Thomas [11] these moments can be obtained from two profile measurements, one taken in the direction of the grain and the other across the grain assuming that both profiles have the same variance

$m_{00}$ . These surface moments are related to the number of zero crossings  $D_0$  and extrema (minima and maxima)  $D_e$  per unit length of profile by the following equations given by Nayak [16]:

$$\begin{aligned} D_0 \text{ (along grain)} &= \frac{1}{\pi} \left(\frac{m_{20}}{m_{00}}\right)^{1/2}, \\ D_0 \text{ (across grain)} &= \frac{1}{\pi} \left(\frac{m_{02}}{m_{00}}\right)^{1/2}, \\ D_e \text{ (along grain)} &= \frac{1}{\pi} \left(\frac{m_{40}}{m_{00}}\right)^{1/2}, \\ D_e \text{ (across grain)} &= \frac{1}{\pi} \left(\frac{m_{04}}{m_{00}}\right)^{1/2}. \end{aligned} \quad (12)$$

Assuming, for example, the bandwidth parameters  $\alpha_1$  and  $\alpha_2$  set equal to 3 and the value of  $m_{04}/m_{40} = 6561 = 9^4$ , the profile in the direction of the grain will have an average of one ninth of the number of zero-crossings and extrema of those across the grain. No experimental data are available to provide the mean square slopes ( $m_{20}, m_{02}$ ) and the mean square curvatures ( $m_{40}, m_{04}$ ) for anisotropic surfaces. Throughout the study we consider the fictitious data related to the spectral moments given previously by McCool [48] and Bush *et al.* [19].

Furthermore, the random variables involved in (1) are written in non-dimensionalized form as follows:

$$\begin{aligned} \omega_1 &= \frac{\xi_1}{\sqrt{m_{00}\mu}}, & \omega_4 &= -\frac{\xi_4}{\sqrt{m_{40}\mu}}, \\ \omega_6 &= -\frac{\xi_6}{\sqrt{m_{04}\mu}}. \end{aligned} \quad (13)$$

It is noted that necessary condition for the existence of relative maximum (not a saddle point) of the summit at the point  $z(x, y)$  requires that the slopes of a summit  $\xi_2$  and  $\xi_3$  must be zero and the principal curvatures  $\xi_4$  and  $\xi_6$  must be negative, i.e.  $\xi_2 = 0, \xi_3 = 0, \xi_4 \leq 0, \xi_6 \leq 0$  and  $\xi_4 \xi_6 - \xi_5 \geq 0$ .

Using (7) and (8) the probability that an ordinate is a summit of height  $\omega_1$  and curvatures  $\omega_4$  and  $\omega_6$  is now

$$p(\omega_1, \omega_4, \omega_6) = \frac{\mu^2}{(2\pi)^{5/2}} \frac{\sqrt{m_{04}m_{40}}}{\sqrt{m_{02}m_{20}}} |\omega_4 \omega_6| \exp(-X/2), \quad (14)$$

where

$$\begin{aligned} X &= \omega_1^2 + (1 - \beta_2)\omega_4^2 + (1 - \beta_1)\omega_6^2 - 2\sqrt{\beta_1}\omega_1\omega_6 \\ &\quad - 2\sqrt{\beta_2}\omega_1\omega_4 + 2\sqrt{\beta_1\beta_2}\omega_4\omega_6. \end{aligned} \quad (15)$$

In the theory which follows the probability distribution of summits is needed. To obtain it, (14) must be normalized by the ratio of summits to ordinates. The probability that an

ordinate is a summit,  $D_{sum}$ , is found by integrating (14) over the standardized height  $\omega_1$  and the curvatures  $\omega_4$  and  $\omega_6$

$$D_{sum} = \int_0^{+\infty} \int_{-\infty}^{+\infty} \int_{-\infty}^{+\infty} p(\omega_1, \omega_4, \omega_6) d\omega_6 d\omega_4 d\omega_1. \quad (16)$$

According to Bush, Gibson and Koegh [19] the closed form of the density of summits is

$$D_{sum} = \frac{1}{(2\pi)^2} \left( \frac{m_{40}m_{04}}{m_{20}m_{02}} \right)^2. \quad (17)$$

This formula can be also taken as an ordinary check in the numerical evaluation of integrals (16). Finally, dividing (14) by (17) we obtain the joint probability density function of summits as

$$p_{sum}(\omega_1, \omega_4, \omega_6) = \frac{\mu^2}{\sqrt{2\pi}} \left( \frac{m_{04}m_{40}}{m_{02}m_{20}} \right)^{3/2} |\omega_4\omega_6| \exp(-X/2). \quad (18)$$

### 3 Elastic Contact

In the model a cap of each asperity is replaced by a paraboloid having the same height and principal curvatures as the summit of the asperity. The asperities are parameterised by their height  $\xi_1$  and the semiaxes  $a$  and  $b$  of the ellipse obtained from the intersection of the asperity and a plane at height  $h$  above the point  $(x_0, y_0)$  on the mean plane of the rough surface as shown in Fig. 2. The equation for an elliptic paraboloid asperity of summit height  $\xi_1$  above the point  $x_0$  and  $y_0$  is

$$\frac{\xi_1 - z}{\xi_1 - h} = \frac{(x - x_0)^2}{a^2} + \frac{(y - y_0)^2}{b^2}. \quad (19)$$

Differentiating the above equation with respect to  $x$  and  $y$  yields the following relationships between the curvature and the semi-axes  $a$  and  $b$ , see, (1)

$$\xi_4 = \frac{-2(\xi_1 - h)}{a^2}, \quad \xi_6 = \frac{-2(\xi_1 - h)}{b^2}. \quad (20)$$

Using (13) and (20), the semiaxes of the ellipse  $a$  and  $b$  can be expressed as functions of  $\omega_1, \omega_4$  and  $\omega_6$  by the following expressions

$$a^2 = \frac{2(\omega_1\sqrt{m_{00}\mu} - h)}{\omega_4\sqrt{m_{40}\mu}}, \quad b^2 = \frac{2(\omega_1\sqrt{m_{00}\mu} - h)}{\omega_6\sqrt{m_{04}\mu}}. \quad (21)$$

Based on this asperity model, the cross-sectional area per unit nominal area, called the bearing area  $A_G$  is then

$$A_G(s) = \int_{\omega_1=l}^{\infty} \int_{\omega_4=0}^{\infty} \int_{\omega_6=0}^{\infty} \pi ab \times p_{sum}(\omega_1, \omega_4, \omega_6) d\omega_6 d\omega_4 d\omega_1, \quad (22)$$

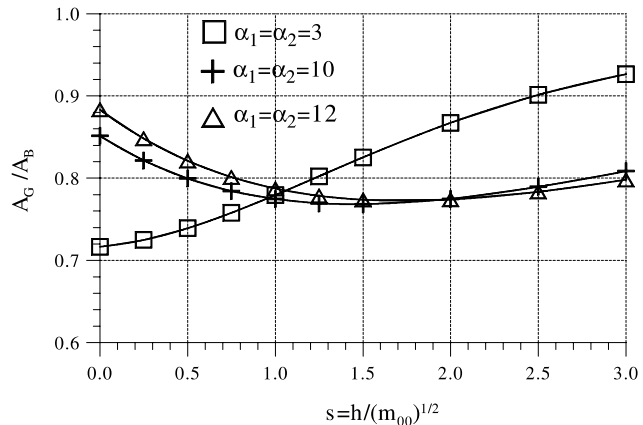


**Fig. 3** The variation of  $A_G/A_B$  with separation  $s = (h/\sqrt{m_{00}})$  for various bandwidth parameters  $\alpha_1$  and  $\alpha_2$ :  $m_{00} = 3.$ ,  $m_{20} = 1.$ ,  $m_{02} = 81.$ ,  $m_{40} = 1.$ ,  $m_{04} = 6561.$  (squares),  $m_{00} = 12.$ ,  $m_{20} = 1.$ ,  $m_{02} = 81.$ ,  $m_{40} = 1.$ ,  $m_{04} = 6561.$  (triangles),  $m_{00} = 0.0625$ ,  $m_{20} = 8. \times 10^{-5}$ ,  $m_{02} = 8. \times 10^{-4}$ ,  $m_{40} = 1.04 \times 10^{-6}$ ,  $m_{04} = 1.04 \times 10^{-4}$  (crosses)

where

$$l = \frac{s}{\sqrt{\mu}}, \quad s = \frac{h}{\sqrt{m_{00}}}. \quad (23)$$

The bearing area (or Abbott-Firestone bearing area) can be understood by imagining a straight smooth plane being brought slowly down towards the profile of the surface under investigation.

Using (21) and (22) the bearing area  $A_G$  becomes

$$A_G(s) = \frac{\mu^2(\alpha_1\alpha_2)^{1/4}}{(2\pi)^{3/2}} \int_l^{\infty} \int_0^{\infty} \int_0^{\infty} (\omega_4\omega_6)^{1/2} (\omega_1 - l) \times \exp(-1/2X) d\omega_6 d\omega_4 d\omega_1. \quad (24)$$

The bearing area  $A_B$  corresponding the Greenwood-Williamson [1] isotropic model is given by the integral

$$A_B(h) = \frac{1}{\sqrt{2\pi m_{00}}} \int_h^{\infty} \exp\left(\frac{-z^2}{2m_{00}}\right) dz. \quad (25)$$

The bearing area based on this asperity model can be compared with the true bearing area as a test of the validity of the model for strongly anisotropic surfaces. In Fig. 3 the ratio  $A_G/A_B$  is plotted against  $s$  for various bandwidth parameters  $\alpha_1$  and  $\alpha_2$  taken from (11). For large separations the ratio  $A_G/A_B$  tends to 1.

The bearing area is a useful tool in characterising a large group of surfaces of some practical importance. Many technical surfaces employed in machine joints are not produced in a single operation but in a sequence of machining operations. Such a sequence of operations superimposed on an earlier surface remove the higher parts of asperities of the original process and produce a finer texture leaving the deep valleys of the initial process untouched. It results in

increasing the mean peak radius even more and reducing the plasticity index [1]. Such processes are termed multi-process or stratified surfaces (see Reference [40]) and their height distributions may contain useful information needed to categorise the surface multifinish profiles for quality control purposes.

The elastic deformation of the asperity causes the contact ellipse to be smaller than the geometric ellipse. If the contact ellipse has the semiaxes  $A$  and  $B$  then these are related to the semiaxes of the geometric ellipse  $a$  and  $b$  by the following equation (Bush *et al.* [19])

$$\frac{A^2}{a^2} + \frac{B^2}{b^2} = 1 \tag{26}$$

and

$$\lambda^2 = \frac{b^2}{a^2} = \frac{kK - (1 - k^2) \frac{dK}{dk}}{\frac{dK}{dk}}, \tag{27}$$

where  $a$  and  $b$  denote the semiminor and the semimajor axes of the ellipse obtained from the intersection of the asperity (elliptical paraboloid) and a plane at height  $h$ , respectively making zero angles with the positive  $x$ -axis.  $K$  is the complete elliptic integral of the first kind

$$K(e) = \int_0^{\pi/2} (1 - e^2 \sin^2 \phi)^{-1/2} d\phi \tag{28}$$

of the argument  $e$  (eccentricity of the ellipse) defined as

$$e^2 = 1 - (B/A)^2. \tag{29}$$

To express  $A$  and  $B$  ( $B < A$ ) as functions of  $\omega_1$ ,  $\omega_4$  and  $\omega_6$  the assumption of highly eccentric ellipses (small  $b/a$  and, correspondingly,  $m_{40} \ll m_{04}$ ) allows a considerable simplification of (27). Let

$$e_1 = \frac{B}{A} = \sqrt{1 - e^2} \tag{30}$$

and using as in Bush *et al.* [19] the following small  $e_1$  expansion for  $K$

$$K(e) = \ln\left(\frac{4}{e_1}\right) + \frac{e_1^2}{4} \ln\left(\frac{4}{e_1}\right) - \frac{e_1^2}{4} \tag{31}$$

(27) becomes

$$\lambda^2 = e_1^2 \left[ \ln\left(\frac{4}{e_1}\right) - 1 \right]. \tag{32}$$

This relation between  $\lambda$  and  $e_1$  can be inverted numerically (see, Bush *et al.* [19]) to yield the following approximate relation between them

$$e_1 = \frac{0.4777\lambda}{1 - 1.3211\lambda}. \tag{33}$$

Thus, (26) can be rewritten in the form

$$A = \frac{a\lambda}{(\lambda^2 + e_1^2)^{1/2}} \tag{34}$$

and

$$B = \frac{a\lambda e_1}{(\lambda^2 + e_1^2)^{1/2}}. \tag{35}$$

The semiaxes of the ellipse  $a$  and  $b$  and the value  $\lambda$  can be found from (21) and (27).

In the following, we will use the complete elliptic integrals of the first and second kind,  $K$  and  $E$ , respectively, in the form of the polynomial approximations (see, Abramowitz and Stegun [55])

$$K(e) = (a_0 + a_1 m_1 + a_2 m_1^2) + (b_0 + b_1 m_1 + b_2 m_1^2) \ln(1/m_1) + \epsilon(m) \tag{36}$$

with error  $|\epsilon(m)| \leq 3 \cdot 10^{-5}$ ,

$$\begin{aligned} a_0 &= 1.3862944, & b_0 &= 0.5, \\ a_1 &= 0.1119723, & b_1 &= 0.1213478, \\ a_2 &= 0.0725296, & b_2 &= 0.0288729 \end{aligned} \tag{37}$$

and

$$E(e) = (1 + a_1 m_1 + a_2 m_1^2) + (b_1 m_1 + b_2 m_1^2) \ln(1/m_1) + \epsilon(m) \tag{38}$$

with error  $|\epsilon(m)| \leq 4 \cdot 10^{-5}$ ,

$$\begin{aligned} a_1 &= 0.4630151, & b_1 &= 0.2452727, \\ a_2 &= 0.10778112, & b_2 &= 0.0412496. \end{aligned} \tag{39}$$

In the above equations the parameter  $m$  is defined as

$$m = e^2 \tag{40}$$

while the complementary parameter  $m_1$  is defined by

$$m + m_1 = 1. \tag{41}$$

(Other approximate formulas for elliptic integral of the first and second kind are available in the papers of Brewe and Hamrock [56], Dyson *et al.* [57], and Greenwood [58].)

When the bodies are pressed together displacements will occur in both of them. Motivated by the fact that the normal displacements within the loaded region at any point in one body is inversely proportional to the plane-strain modulus  $E/(1 - \nu^2)$  (for details we refer to Johnson [59]) and using the theory of superposition it can be shown that the sum of elastic normal displacements will be proportional to

the harmonic (in tribology literature called also effective or contact) elastic modulus  $E^*$  defined by

$$\frac{1}{E^*} = \frac{1 - \nu_1^2}{E_1} + \frac{1 - \nu_2^2}{E_2}, \tag{42}$$

where  $E_1, E_2, \nu_1$  and  $\nu_2$  are the elastic moduli and the Poisson ratios for both the contacting bodies, respectively. Therefore, if one of contacting surfaces is much more elastic than the other,  $E^*$  is just the plane-strain modulus  $E/(1 - \nu^2)$ ; if the materials are the same,  $E^*$  is one half of it. For the purposes of this analysis contact between two rough unflat surfaces is equivalent to contact between a single deformable rough surface while the second surface is considered to be a rigid and smooth flat plane. Hence, the deformable body is described by the effective modulus  $E^*$  and mean effective radius  $R_m$  expressed as  $R_m = (R' + R'')^{1/2}$ , where  $R'$  and  $R''$  are defined as the principal relative radii of curvature of each surface [59].

We introduce the mean effective radius of a single asperity of curvature  $R_m$  (or mean summit curvature  $\kappa_m$ ) as follows:

$$1/R_m = \kappa_m = \frac{|\xi_4 + \xi_6|}{2}, \tag{43}$$

where  $\xi_4$  and  $\xi_6$  are the curvatures in the two orthogonal directions. In comparison with the usual assumption that the asperity deformation is localized mainly in the vicinity of the contact, an alternative, more realistic approach can be adopted in which the values of curvatures may change during the process of asperity deformation. Using (20) and (21), the mean curvature  $\kappa_m$  can be expressed as functions of  $\omega_6$  and  $\lambda$  from (32), so (43) becomes

$$\kappa_m = \frac{1}{2} \omega_6 \sqrt{\mu m_{04}} (1 + \lambda^2). \tag{44}$$

From the theory of elasticity the following expressions may be written in terms of the approach  $\omega$  given by

$$\omega = \xi_1 - h \tag{45}$$

for the elastic contact area  $A_i$  and the elastic load  $W_i$  of the individual asperity [59]:

$$\begin{aligned} A_i(\omega) &= \left( \frac{E(e)}{K(e)(1 - e^2)^{1/2}} \right) \pi R_m \omega \\ &= f_1(e) \pi (1/\kappa_m) \omega \end{aligned} \tag{46}$$

and

$$\begin{aligned} W_i(\omega) &= \left( \frac{\pi E(e)^{1/2}}{2K(e)^{3/2}(1 - e^2)^{1/2}} \right) \frac{4}{3} E^* R_m^{1/2} \omega^{3/2} \\ &= f_2(e) \frac{4}{3} E^* (1/\kappa_m)^{1/2} \omega^{3/2}, \end{aligned} \tag{47}$$

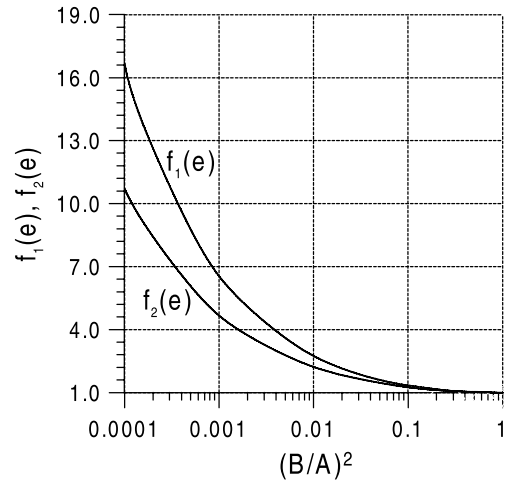


Fig. 4 Plots of the function  $f_1(e)$  and  $f_2(e)$

where  $f_1(e)$  and  $f_2(e)$  are the deviations from the circular contact model and elliptic one for contact area and contact load, respectively,  $\kappa_m$  is the mean curvature calculated by (44).  $E(e)$  denotes the complete elliptic integral of the second kind of the argument  $e$

$$E(e) = \int_0^{\pi/2} (1 - e^2 \sin^2 \phi)^{1/2} d\phi \tag{48}$$

which can be approximated by (38). Plots of the function  $f_1(e)$  and  $f_2(e)$  in Fig. 4 can be valuable to visualize the influence of eccentricity  $e$  on the contact area and the load in (46) and (47), respectively. For circular model ( $A = B$ ),  $f_1(e) = f_2(e) = 1$ , and (46) and (47) give the Hertz expressions for isotropic elastic contact.

*Remark* In another way the elastic contact area  $A_i$  can be written as the function of the semiaxes of the contact ellipse  $A$  and  $B$  from (34) and (35) in the following form:  $A_i(\lambda) = \pi AB$ .

If the surfaces come together until their reference planes are separated by the distance  $h$ , then all asperities are in contact if height  $\xi_1$  exceeds the separation  $h$ . Thus, the probability of making contact at any summit of dimensionless height  $\omega_1 = (\xi_1/\sqrt{m_{00}\mu})$  with given nondimensionalized curvatures  $\omega_4$  and  $\omega_6$  is

$$\begin{aligned} P(l) &\equiv \text{Prob}(\omega_1 > l) \\ &= \int_l^\infty \int_0^\infty \int_0^\infty p_{sum}(\omega_1, \omega_4, \omega_6) d\omega_6 d\omega_4 d\omega_1. \end{aligned} \tag{49}$$

If there are  $N$  summits in all, the expected number of summits above a given height  $\omega_1$  can be calculated for the normalized separation,  $l = h/\sqrt{m_{00}\mu}$  (see (23)) as

$$n(l) = N \int_l^\infty \int_0^\infty \int_0^\infty p_{sum}(\omega_1, \omega_4, \omega_6) d\omega_6 d\omega_4 d\omega_1, \tag{50}$$

where  $N$  denotes the total number of summits equal to

$$N = D_{sum}A_0. \tag{51}$$

Here,  $A_0$  describes the nominal contact area while the density of summits  $D_{sum}$  is determined by (17). The nominal contact area  $A_0$  will be considered later as a part nominal area corresponding to an area of the zero-thickness contact finite element used.

For  $\omega = (\xi_1 - h)$  and  $A_i(\omega)$  given in (46) the mean contact area is

$$A_e(l) = \pi D_{sum}A_0\sqrt{m_{00}\mu} \int_l^\infty \int_0^\infty \int_0^\infty f_1(e)(\omega_1 - l)(1/\kappa_m) \times p_{sum}(\omega_6, \omega_4, \omega_1) d\omega_6 d\omega_4 d\omega_1. \tag{52}$$

Similarly, with the help of (47) we can find the expected (elastic) load as

$$W_e(l) = \frac{4}{3}D_{sum}A_0E^*(m_{00}\mu)^{3/4} \times \int_l^\infty \int_0^\infty \int_0^\infty f_2(e)(\omega_1 - l)^{3/2}(1/\kappa_m)^{1/2} \times p_{sum}(\omega_6, \omega_4, \omega_1) d\omega_6 d\omega_4 d\omega_1. \tag{53}$$

The integrals (52) and (53) have been evaluated numerically using Gauss–Legendre 50-point quadrature formula for various separations and surface moments. (It is of interest to note that a larger number of integrating points have no influence on results.)

For purely elastic contact the results of the contact area and nominal pressure for the strongly anisotropic model are compared with equivalent Greenwood–Williamson approximation for anisotropic case (for details we refer to Reference [48]). The results obtained for various bandwidth parameters  $\alpha$  are given in Tables 1 and 2. In respect to the elastic contact area there is rather good agreement between the two models. The difference in the nominal pressure are significant at lower values of  $\alpha$  while at higher values of  $\alpha$  the equivalent GW model affords an encouraging good approximation.

#### 4 Elastic Normal Contact Stiffness

The coefficient of the normal stiffness for two asperities can be obtained by differentiating (47) with respect to approach  $w$

$$k_{ni} = 2f_2(e)E^*(1/\kappa_m)^{1/2}\omega^{1/2}. \tag{54}$$

The normal elastic stiffness for the joint is obtained by integrating (54) for all the summits in contact, thus

$$K_n^e = 2D_{sum}A_0E^*(m_{00}\mu)^{1/4}$$

**Table 1** Comparison of the strongly anisotropic model at  $\alpha = 10$  and equivalent Greenwood–Williamson (GW) model for the anisotropic case;  $m_{00} = 0.0625, m_{20} = 8. \times 10^{-5}, m_{02} = 8. \times 10^{-4}, m_{40} = 1.04 \times 10^{-6}, m_{04} = 1.04 \times 10^{-4}, E^* = 1.14 \times 10^5 \text{ N/mm}^2$

$h/m_{00}^{1/2}$	$A_e/A_0$ [%]		$W_e/A_0$ [N/mm <sup>2</sup> ]	
	GW	anisotropic	GW	anisotropic
1.0	5.1497	6.1222	86.5534	93.3897
1.5	2.2210	2.5424	34.1470	36.5963
2.0	0.7908	0.8673	11.1922	11.9003
2.5	0.2286	0.2394	2.9972	3.1613
3.0	0.0529	0.0529	0.6470	0.6778
3.5	0.0097	0.0093	0.1114	0.1162

**Table 2** Comparison of the strongly anisotropic model at  $\alpha = 3$  and equivalent Greenwood–Williamson (GW) model for the anisotropic case;  $m_{00} = 3., m_{20} = 1., m_{02} = 81., m_{40} = 1., m_{04} = 6561., E^* = 1.14 \times 10^5 \text{ N/mm}^2$

$h/m_{00}^{1/2}$	$A_e/A_0$ [%]		$W_e/A_0$ [N/mm <sup>2</sup> ]	
	GW	anisotropic	GW	anisotropic
2.0	1.0525	0.9280	2105.97	2877.81
2.5	0.3185	0.2589	580.16	796.57
3.0	0.0733	0.0570	122.56	175.17
3.5	0.0126	0.0099	19.476	30.435
4.0	0.00159	0.00135	2.2942	4.1568
4.5	0.000146	0.000143	0.1981	0.4397

$$\times \int_l^\infty \int_0^\infty \int_0^\infty f_2(e)(\omega_1 - l)^{1/2}(1/\kappa_m)^{1/2} \times p_{sum}(\omega_6, \omega_4, \omega_1) d\omega_6 d\omega_4 d\omega_1. \tag{55}$$

The same result can be obtained using Leibnitz rule differentiating (53) directly with respect to the interference  $w$  as shown in [51]. We note that for the spherical model  $f_2(e) = 1$  and the (55) gives the normal elastic stiffness obtained for elastic contact of the isotropic surfaces [51].

Alternatively, from (55) and (53) the elastic normal stiffness per unit area can be found as the function of the normal load  $W_e(l)$ . It is given by

$$k_N^e = \frac{3}{2} \frac{W_e(l)}{A_0(m_{00}\mu)^{1/2}} \frac{F_{1/2}(l)}{F_{3/2}(l)}, \tag{56}$$

where the functions  $F_{1/2}(l)$  and  $F_{3/2}(l)$  are related by

$$F_\nu(l) = \int_l^\infty \int_0^\infty \int_0^\infty f_2(e)(\omega_1 - l)^\nu(1/\kappa_m)^{1/2} \times p_{sum}(\omega_6, \omega_4, \omega_1) d\omega_6 d\omega_4 d\omega_1 \tag{57}$$

with the probability density of summits  $p_{sum}$  defined by (18) and  $\nu = 1/2$  or  $\nu = 3/2$ .

### 5 Plastic Contact

The total contact area consists of both the elastic and plastic parts. Therefore, critical interference  $\omega_c$  has to be defined as a critical value at which an asperity deforms from elastic to plastic contact. The analysis of Pullen and Williamson [24] showed that volume beyond a critical value  $\omega_c$  has to be preserved as the plastic deformation proceeds for  $\omega > \omega_c$ . Based on plastic volume conservation, after Horng [26], it can be written that the plastic contact area is

$$A_i^p(\omega) = f_3(e)\pi(1/\kappa_m)\omega \left[ 2 - \frac{\omega_c}{\omega}(2 - f_4(e)) \right], \tag{58}$$

where

$$f_3(e) = \frac{E(e)e^2}{2(1 - e^2)^{1/2}[E(e) - K(e)(1 - e^2)]} \tag{59}$$

and

$$f_4(e) = \frac{2[E(e) - (1 - e^2)K(e)]}{K(e)e^2}. \tag{60}$$

If asperities are spherical summits i.e. ( $a = b$ ),  $f_3(e) = 1$  and  $f_4(e) = 1$  they produce the contact area  $A_i^p = \pi(1/\kappa_m)\omega(2 - \omega_c/\omega)$ , of the Chang *et al.* [25] elastic-plastic microcontact (CEB) model.

In the case when the interference  $\omega$  is much larger than  $\omega_c$  the contact area given by (58) gives a fully plastic area as

$$A_i^p(\omega) = 2\pi(1/\kappa_m)\omega f_3(e). \tag{61}$$

Analytical results obtained by CEB model with the 3-D finite element results (using commercial ABAQUS 6.4 package) for the elasto-plastic frictionless contact of a deformable single spherical summit of radius  $R = 2.448$  [mm] and a rigid flat can make an interesting comparison [52]. First, the material of the sphere was there modelled as elasto-perfectly plastic while in the second, the material of the sphere was considered as elasto-plastic including linear isotropic with the strain-hardening modulus  $h$  of  $0.1E$  and large geometrical deformations. The dimensionless contact load obtained by Chang *et al.* [25] (CEB model) differs from present FE results. It overestimates finite element results at small interferences (see also Kogut and Etsion [32])) and underestimates present results up to 23% (without hardening) and 29% (with hardening and large deformations) at  $\omega/\omega_c = 9$ , respectively. For the elastic-perfectly plastic the difference diminishes at large interferences down to 6.5% at  $\omega/\omega_c = 47$ . For much more realistic assumptions regarding the hardening and large deformations the difference between CEB and FE models increases to 46% at the same dimensionless interference. The corresponding finite results vs CEB model, for the elasto-perfectly plastic and the elasto-plastic with hardening models, at  $\omega/\omega_c = 47$  are

$W/W_c = 149.1$  and  $W/W_c = 205.4$ , respectively, where  $W_c = 88.684$  [N] (see [32] for details). We note that the similar tendency has been recently observed by Kogut and Etsion [32] for the axisymmetric finite element model.

It is known that the initial yielding occurs when the maximum contact pressure  $p_m$  calculated as (cf. (46) and (47))

$$p_m = \frac{3}{2} \frac{W_i^e}{A_i^e} = \frac{\sqrt{K(e)E(e)}}{E^* \sqrt{\kappa_m \omega}} \tag{62}$$

reaches the value

$$p_m = KY, \tag{63}$$

where  $Y$  is the yield strength and  $K$  represents the maximum contact yield coefficient which is a function of Poisson's ratio  $\nu$  only and can be linearly approximated [25] by

$$K = 1.282 + 1.158\nu. \tag{64}$$

Hence, from (62) and (63) the critical value of interference  $\omega_c = (\xi_1 - h)_c$  which causes plastic deformation is

$$\omega_c = K(e)E(e) \left( \frac{KY}{E^*} \right)^2 \frac{1}{\kappa_m}. \tag{65}$$

After experimental data given by Jamari and Schipper [60] the mean contact pressure in fully plastic regime can be related to the hardness  $H$  as

$$p_a = c_h H, \tag{66}$$

where  $c_h$  denotes the hardness coefficient for fully plastic contact regime to be determined based on the experimental results.

The fully plastic contact load is then equal to the fully plastic contact area multiplied by the mean contact pressure. Consequently from (61), the fully plastic load is

$$W_i^p(\omega) = 2\pi(1/\kappa_m)\omega f_3(e)c_h H. \tag{67}$$

An empirical relation between the indentation hardness,  $H$  and the yield strength  $Y$  given by Tabor [62] is

$$Y = 0.354H. \tag{68}$$

After Tabor, assuming  $\nu = 0.3$  plastic flow will occur when the maximum Hertzian pressure  $p_m$  between a ball and a plane reaches about  $p_m = 0.577H$ . However, for elliptical contacts the value for the first yield in the material is not equal to  $0.577H$  but is slightly dependent on the ratio ( $R_y/R_x$ ), where  $R_x$  and  $R_y$  are the principal relative radii of curvature in the  $x$  and  $y$  directions, respectively (for details refer to Wu Chengwei *et al.* [61], Johnson [59], or Greenwood [58]).

The plasticity index  $\psi$  was first introduced by Greenwood and Williamson [1] to be defined by the equation

$$\psi = \sqrt{\sigma \bar{\kappa}_m} \left( \frac{E^*}{H} \right), \tag{69}$$

where  $\sigma$  is the standard deviation of summit heights about the summit mean plane. To express  $\psi$  in terms of the surface moments  $m_{ij}$  the mean summit curvature  $\bar{\kappa}_m$  and the standard deviation of summit heights  $\sigma$  must be calculated in terms of the spectral moments. These were found in Bush, Gibson and Keogh [19] as

$$\begin{aligned} \bar{\kappa}_m &= \int_{-\infty}^{\infty} \int_0^{\infty} \int_0^{\infty} \frac{|\xi_4 + \xi_6|}{2} p(\omega_1, \omega_4, \omega_6) d\omega_6 d\omega_4 d\omega_1 \\ &= \sqrt{\frac{\pi}{8}} (\sqrt{m_{04}} + \sqrt{m_{40}}) \end{aligned} \tag{70}$$

and

$$\begin{aligned} \sigma^2 &= \int_{-\infty}^{\infty} \int_0^{\infty} \int_0^{\infty} (\xi_1 - \delta)^2 \\ &\quad \times p(\omega_1, \omega_4, \omega_6) d\omega_6 d\omega_4 d\omega_1 = cm_{00}, \end{aligned} \tag{71}$$

where

$$c = \left( 2 - \frac{\pi}{2} \right) (\beta_1 + \beta_2) m_{00} \tag{72}$$

and  $\delta$  is the distance between the mean height of the summits and mean level of the surface (or mean surface plane) given as

$$\begin{aligned} \delta &= \int_{-\infty}^{\infty} \int_0^{\infty} \int_0^{\infty} \xi_1 p(\omega_1, \omega_4, \omega_6) d\omega_6 d\omega_4 d\omega_1 \\ &= \left( \frac{m_{00}\pi}{2} \right)^2 (\sqrt{\beta_1} + \sqrt{\beta_2}). \end{aligned} \tag{73}$$

Substituting for  $\sigma$  and  $\bar{\kappa}_m$  into (70), and removing the material constants  $E^*$  and  $KY$ , the critical interference  $\omega_c^*$  expressed in a nondimensional form, becomes

$$(\omega_1 - l) = \omega_c^* = \frac{\sqrt{8c} K(e) E(e) (\sqrt{m_{04}} + \sqrt{m_{40}})}{\pi^{3/2} \omega_6 \mu \sqrt{m_{04}} (1 + \lambda^2) \psi^2}. \tag{74}$$

In the elasto-plastic model the contact area and load of asperities are the sum of the elastic and plastic components. For  $\omega < \omega_c$ , there is a purely elastic deformation to be obtained from (46) and (47). For  $\omega \geq \omega_p$ , the contact area and contact load given by (58) and (67) obtained for fully plastic deformation at the plane when the contact pressure reaches the value of  $c_h H$  should be adopted. We note that no solid expression for the interference  $\omega_p$  required to produce fully plastic deformation is known. Zhao, Maietta and Chang [53] suggest that the minimum value  $\omega_p$  is at least 25 times that at initial yielding  $\omega_c$  or the interference  $\omega_p$  would be using

experimental results at least 54 times that at initial yielding in the case of fully plastic deformation. According to experimental results of Jamari and Schipper [60] the value  $\omega_p/\omega_c$  is almost constant and independent on the shape of the elliptic contact and it has the value of about 45 for brass or 22 for phosphor-bronze. Throughout the study the values of  $c_h = 0.967$  and  $\omega_p/\omega_c = 45$ . were assumed.

### 6 Elasto-Plastic Contact

In the study the approach proposed by Zhao, Maietta and Chang [53] and Jeng and Wang [54] will be used to analyse the elliptic elasto-plastic contact model. These authors proposed a relation between elasto-plastic contact area  $A_{ep}$  and approach  $\omega$ . This relation was modeled by a polynomial smoothly joining the expressions for elastic area  $A_e$  and plastic one  $A_p$ . It is constructed by mapping an appropriate template cubic polynomial segment into quadrilateral bounding the transition region on the  $A_{ep}-\omega$  plane. Zhao *et al.* [53] employed the statistical analysis of spherical indentations of Francis [63] where the mean contact pressure in the elasto-plastic regime may be characterized by a logarithmic function. By using that approach, the mean contact pressure and the contact area are expressed as follows:

$$p_a = c_h H - H \left( c_h - \frac{2}{3} K_v \right) \left( \frac{\ln \omega_p - \ln \omega}{\ln \omega_p - \ln \omega_c} \right) \tag{75}$$

and

$$\begin{aligned} A_i^{e-p}(\omega) &= f_1(e) \pi (1/\kappa_m) \omega \\ &\quad + [2\pi f_3(e) (1/\kappa_m) \omega - \pi f_1(e) (1/\kappa_m) \omega] \\ &\quad \times \left( 3 \frac{\omega - \omega_c}{\omega_p - \omega_c} - 2 \frac{\omega - \omega_c}{\omega_p - \omega_c} \right). \end{aligned} \tag{76}$$

Based on von Mises failure criteria  $K_v$  in (75) is related to the Poisson's ratio  $\nu$  as [60]:

$$K_v = 0.454 + 0.41\nu.$$

The contact load is equal to the contact area  $A_i^{e-p}$  multiplied by the mean contact pressure,  $p_a$ , so

$$\begin{aligned} W_i^{ep}(\omega) &= \left[ \pi f_1(e) (1/\kappa_m) \omega \right. \\ &\quad + [2\pi f_3(e) (1/\kappa_m) \omega - \pi f_1(e) \omega (1/\kappa_m)] \\ &\quad \times \left( 3 \frac{\omega - \omega_c}{\omega_p - \omega_c} - 2 \frac{\omega - \omega_c}{\omega_p - \omega_c} \right) \left. \right] \\ &\quad \times \left[ c_h H - H \left( c_h - \frac{2}{3} K_v \right) \left( \frac{\ln \omega_p - \ln \omega}{\ln \omega_p - \ln \omega_c} \right) \right]. \end{aligned} \tag{77}$$

Therefore, after introducing the nondimensional variables, the total contact area consists of the elastic, elasto-plastic and plastic parts

$$A(l) = A^e(l) + A^{ep}(l) + A^p(l) \tag{78}$$

with the elastic area

$$A^e(l) = \pi D_{sum} A_0 \sqrt{m_{00} \mu} \times \int_l^{(l+\omega_c^*)} \int_0^\infty \int_0^\infty f_1(\omega)(\omega_1 - l)(1/\kappa_m) \times p_{sum}(\omega_6, \omega_4, \omega_1) d\omega_6 d\omega_4 d\omega_1 \tag{79}$$

the elasto-plastic area

$$A^{ep}(l) = \pi D_{sum} A_0 \sqrt{m_{00} \mu} \times \int_{(l+\omega_c^*)}^{(l+\omega_p^*)} \int_0^\infty \int_0^\infty f_1(e)(1/\kappa_m)\omega + [2f_3(e)(1/\kappa_m)\omega - f_1(e)\omega] \times \left(3 \frac{\omega - \omega_c}{\omega_p - \omega_c} - 2 \frac{\omega - \omega_c}{\omega_p - \omega_c}\right) \times p_{sum}(\omega_6, \omega_4, \omega_1) d\omega_6 d\omega_4 d\omega_1 \tag{80}$$

and the plastic one

$$A^p(l) = 2\pi D_{sum} A_0 \sqrt{m_{00} \mu} \int_{(l+\omega_p^*)}^\infty \int_0^\infty \int_0^\infty f_3(e)(\omega_1 - l) \times p_{sum}(\omega_6, \omega_4, \omega_1) d\omega_6 d\omega_4 d\omega_1. \tag{81}$$

Similarly, the total load can be split into

$$W(l) = W^e(l) + W^{ep}(l) + W^p(l), \tag{82}$$

where

$$W^e(l) = \frac{4}{3} D_{sum} A_0 E^*(m_{00} \mu)^{3/4} \times \int_l^{(l+\omega_c^*)} \int_0^\infty \int_0^\infty f_2(e)(\omega_1 - l)^{3/2}(1/\kappa_m)^{1/2} \times p_{sum}(\omega_6, \omega_4, \omega_1) d\omega_6 d\omega_4 d\omega_1, \tag{83}$$

$$W^{ep}(l) = \pi D_{sum} A_0 \sqrt{m_{00} \mu} \times \int_{(l+\omega_c^*)}^{(l+\omega_p^*)} \int_0^\infty \int_0^\infty [f_1(e)(1/\kappa_m) + [2f_3(e)(1/\kappa_m) - f_1(e)]] \times \left[3 \left(\frac{\omega - \omega_c}{\omega_p - \omega_c}\right)^2 - 2 \left(\frac{\omega - \omega_c}{\omega_p - \omega_c}\right)^3\right] \times \left[ c_h H - H \left( c_h - \frac{2}{3} K_v \right) \left( \frac{\ln \omega_p - \ln \omega}{\ln \omega_p - \ln \omega_c} \right) \right] \times (\omega_1 - l) p_{sum}(\omega_6, \omega_4, \omega_1) d\omega_6 d\omega_4 d\omega_1 \tag{84}$$

and

$$W^p(l) = 2\pi D_{sum} A_0 \sqrt{m_{00} \mu} c_h H \times \int_{(l+\omega_p^*)}^\infty \int_0^\infty \int_0^\infty f_3(e)(1/\kappa_m)(\omega_1 - l) \times p_{sum}(\omega_6, \omega_4, \omega_1) d\omega_6 d\omega_4 d\omega_1, \tag{85}$$

where the mean summit curvature of a single asperity  $\kappa_m$  is given by (44) and  $\omega_c^*$  from (74) defines the critical interference which can be now rewritten as

$$\omega_c^* = \frac{\gamma}{\omega_6}, \tag{86}$$

where (cf. (74))

$$\gamma = \frac{\sqrt{8c} K(e) E(e) (\sqrt{m_{04}} + \sqrt{m_{40}})}{\pi^{3/2} \mu \sqrt{m_{04}} (1 + \lambda^2) \psi^2}. \tag{87}$$

The variation of the plastic contact area  $A^p/A$  and the dimensionless mean contact pressure  $W/AH$  with the plasticity index  $\psi$  are presented in Figs. 5 and 6. As can be seen from the Fig. 5 at small values of  $\psi$  the ratio  $A^p/A$  is very small even for the largest load. Only for small values of  $\psi$  the surface remains elastic. For  $\psi > 1$  plastic flow will occur even at a very small load. Figure 6 presents the dimensionless mean contact pressure  $W/AH$  as the function of the dimensionless load  $W/(HA_0)$  for various values of plasticity index  $\psi$ . The ratio  $W/AH$  represents the real mean contact pressure  $W/A$  normalized by the indentation hardness  $H$ . It is clear from Fig. 5 that for the greater value of  $\psi$  by given value of load (or separation) the degree of plastic deformation is dominant; that effect increases as the separation of surfaces becomes smaller (large separation means that there is little contact). At high values of  $\psi$  the normalized contact pressure  $W/AH$  approaches the value  $(2/3)p_m = 0.354H$  which corresponds to the average contact pressure at the inception of plastic deformation (see (68)).

We note after Greenwood and Williamson [1] that for most surfaces the mode of deformation is almost independent of load. It is elastic if the plasticity index is low and plastic if it is high. The idea that in general contact is elastic at low loads and becomes plastic as the load increases is not true. Sharp asperities would deform plastically even under lightest loads, while blunt asperities would deform elastically even under heaviest loads. When  $\psi$  exceeds 1 plastic flow will occur even at trivial nominal pressures and when  $\psi < 0.6$  plastic contact can be caused only under very large nominal pressures. In the region  $0.6 < \psi < 1$  the mode of deformation is dependent on the load. The results to be found in Bush *et al.* [19] show that the deformation for the anisotropic surface will be plastic for  $\psi > 0.7$ , elastic for  $\psi < 0.5$  and for the intermediate region in the range  $0.5 < \psi < 0.7$  the mode of deformation is dependent on the load.

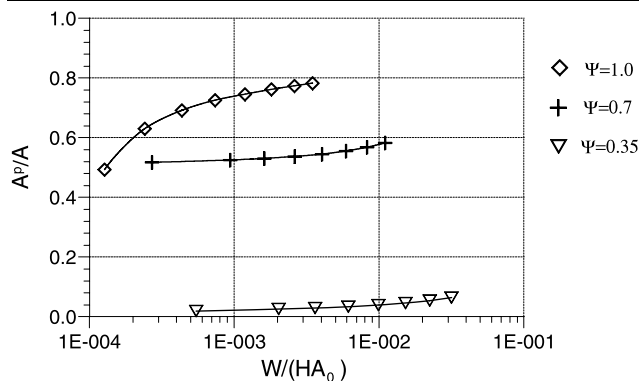


**Fig. 5** Plastic portion of the real contact area  $A^p/A$  vs. dimensionless contact load  $W/HA_0$  for different values of the plasticity index  $\psi$ ;  $m_{00} = 0.0625, m_{20} = 8. \times 10^{-5}, m_{02} = 8. \times 10^{-4}, m_{40} = 1.04 \times 10^{-6}, m_{04} = 1.04 \times 10^{-4}, E^* = 1.14 \times 10^5 \text{ N/mm}^2, Y = 2070 \text{ N/mm}^2, K = 1.62., c_h = 0.967, \omega_p/\omega_c = 45.$

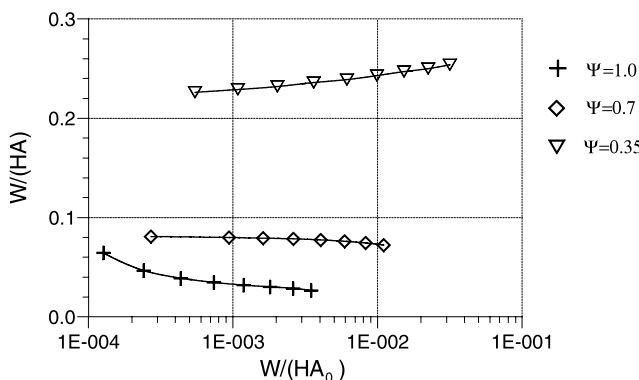


**Fig. 6** Dimensionless real contact pressure  $W/HA$  vs. dimensionless contact load  $W/HA_0$  for different values of the plasticity index  $\psi$ ;  $m_{00} = 0.0625, m_{20} = 8. \times 10^{-5}, m_{02} = 8. \times 10^{-4}, m_{40} = 1.04 \times 10^{-6}, m_{04} = 1.04 \times 10^{-4}, E^* = 1.14 \times 10^5 \text{ N/mm}^2, Y = 2070 \text{ N/mm}^2, K = 1.62., c_h = 0.967, \omega_p/\omega_c = 45.$

From results given by Kogut and Etsion [64] it can be seen that at  $\psi = 2$  only 5% of asperities deform plastically and the yielded part of the real contact area  $A_p/A$  is still very small even for the largest load. Their conclusion is different from the one drawn by authors cited above and is also clearly contrary to the present results that for greater value of  $\psi$  the degree of plastic deformation is dominant. It should be noted, however, that in the present model the critical interference  $\omega_c^*$  from (72) and the limits of all integrals are the functions of the nondimensional curvature (see (13) and 20)) defined by

$$\omega_6 = \frac{2(\xi_1 - h)}{b^2 \sqrt{m_{04}\mu}}$$

which changes systematically due to the deformation of asperities.

### 7 Elasto-Plastic Normal Contact Stiffness

The elastic normal stiffness (see (55)) is valid as long as the plastic deformation of asperities is not considered; otherwise, the stiffness of the elasto-plastic contact has to be calculated using Leibnitz rule differentiating of (82) directly with respect to the interference  $w$  as shown in [51]. This differentiating is now more complicated because the derivation involves an integral with the interchange of the limits within the integral. We have for all the summits in contact

$$\begin{aligned}
 K_n^{ep} &= 2D_{sum}A_0E^*(m_{00}\mu)^{1/4} \\
 &\times \int_l^{(l+\omega_c^*)} \int_0^\infty \int_0^\infty f_2(e)(\omega_1 - l)^{1/2}(1/\kappa_m)^{1/2} \\
 &\times p_{sum}(\omega_6, \omega_4, \omega_1) d\omega_6 d\omega_4 d\omega_1 \\
 &- \frac{4}{3}D_{sum}A_0E^*(m_{00}\mu)^{1/4} \\
 &\times \int_0^\infty \int_0^\infty f_2(e)(\omega_1 - l)^{1/2}(1/\kappa_m)^{1/2} \\
 &\times p_{sum}(\omega_6, \omega_4, l + \omega_c^*) d\omega_6 d\omega_4 \\
 &+ \left[ c_h H - H\left(c_h - \frac{2}{3}K_v\right) \right] \pi D_{sum}A_0 \\
 &\times \int_{(l+\omega_c^*)}^{(l+\omega_p^*)} \int_0^\infty \int_0^\infty [f_1(e)(1/\kappa_m) \\
 &+ [2f_3(e)(1/\kappa_m) - f_1(e)]] \\
 &\times \left[ 3\left(\frac{(\omega_1 - l) - \omega_c^*}{\omega_p^* - \omega_c^*}\right)^2 - 2\left(\frac{(\omega_1 - l) - \omega_c^*}{\omega_p^* - \omega_c^*}\right)^3 \right] \\
 &\times \left[ \frac{\ln \omega_p^* - \ln(\omega_1 - l)}{\ln \omega_p^* - \ln \omega_c^*} - \frac{1}{\ln \omega_p^* - \ln \omega_c^*} \right] \\
 &\times p_{sum}(\omega_6, \omega_4, \omega_1) d\omega_6 d\omega_4 d\omega_1 \\
 &+ 2\pi D_{sum}A_0 c_h H \int_{l+\omega_p^*}^\infty \int_0^\infty \int_0^\infty f_3(e) (1/\kappa_m) \\
 &\times p_{sum}(\omega_6, \omega_4, \omega_1) d\omega_6 d\omega_4 d\omega_1 \\
 &+ 2\pi D_{sum}A_0 c_h H \int_0^\infty \int_0^\infty f_3(e) \omega_p^*(1/\kappa_m) \\
 &\times p_{sum}(\omega_6, \omega_4, l + \omega_c^*) d\omega_6 d\omega_4. \tag{88}
 \end{aligned}$$

The numerical results concerning the elastic (see (55)) and elasto-plastic (see (88)) stiffness coefficients are shown in Figs. 7 and 8 which present the dependence of the normal stiffness coefficients on the average pressure (the total load  $W$  per nominal area  $A_0$ ) for different values of the variance of the surface height  $m_{00}$  and the same value of the plasticity index  $\psi = 0.35$  and  $\psi = 0.5$ , respectively. For both the cases it can be seen that for higher values of  $m_{00}$  which corresponds the higher roughness of the surface the contact stiffness is smaller. A significant difference between the

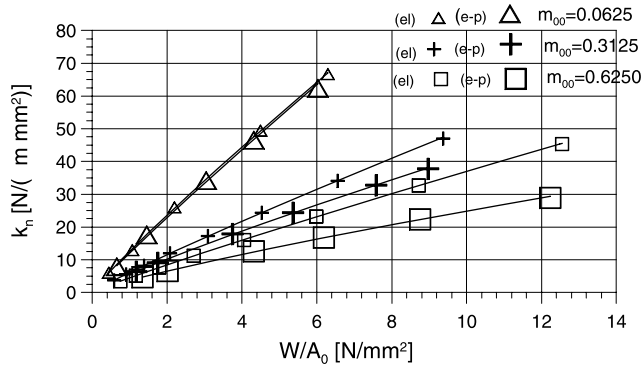


**Fig. 7** Variation of the elastic and elasto-plastic normal stiffness with average pressure for different values of variances of surface height:  $m_{00} = 0.0625$  (triangles),  $m_{00} = 0.3125$  (crosses),  $m_{00} = 0.625$  (squares); ( $m_{20} = 8. \times 10^{-5}$ ,  $m_{02} = 8. \times 10^{-4}$ ,  $m_{40} = 1.04 \times 10^{-6}$ ,  $m_{04} = 1.04 \times 10^{-4}$ ,  $E^* = 1.14 \times 10^5$  N/mm<sup>2</sup>,  $Y = 2070$  N/mm<sup>2</sup>,  $K = 1.62$ ,  $\psi = 0.35$ ,  $c_h = 0.967$ ,  $\omega_p/\omega_c = 45$ .)

elastic and elasto-plastic normal stiffness for the high normal pressure is observed. In comparison to the elastic approach, the stiffness curves obtained for the elasto-plastic model always underestimate them which agrees with experimental observation. The decrease in the elasto-plastic stiffness could be explained in terms of an increase in plastic deformation that has taken place. It was also found that the standard deviation of curvatures had no observable effects on the elastic normal stiffness.

Additionally, the contact stiffness is very sensitive to the plasticity index  $\psi$  increasing sharply as the plasticity index  $\psi$  decreases what is contrary to the results obtained by an elasto-plastic Hornig model [52] and observation made by Kogut Etsion [64] where the authors reported that the contact stiffness was practically insensitive to the plasticity index  $\psi$ . There is a significant difference between the present and the above cited models at very high contact load.

It could be emphasized that the theoretical expressions for the normal contact stiffness are in close agreement with those experimentally measured by Shoukry (see [65]).

## 8 Interface Model for 3D-Frictional Problems

### 8.1 Orthotropic Hardening Model [66]

An important factor is the modelling of orthotropic dry friction between two surfaces. Dry friction which depends on the direction of sliding is called the anisotropic friction. A deviation of the friction force from the direction of sliding is a typical feature of systems with the anisotropic friction (for the isotropic friction the friction forces are always opposite to the slip direction). In the case in which the principal directions are mutually orthogonal the anisotropic friction is called orthotropic. Measurements of the effect of sliding

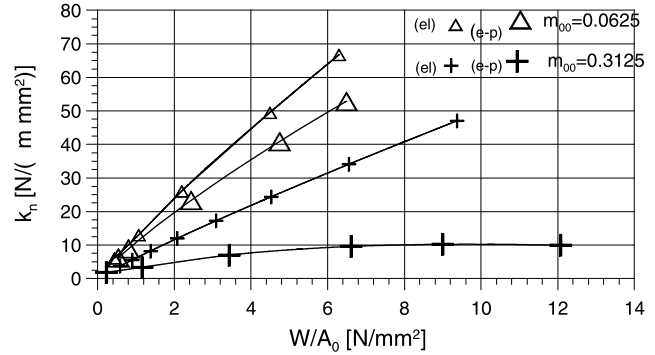


**Fig. 8** Variation of the elastic and elasto-plastic normal stiffness with average pressure for different values of variances of surface height:  $m_{00} = 0.0625$  (triangles),  $m_{00} = 0.3125$  (crosses),  $m_{00} = 0.625$  (squares); ( $m_{20} = 8. \times 10^{-5}$ ,  $m_{02} = 8. \times 10^{-4}$ ,  $m_{40} = 1.04 \times 10^{-6}$ ,  $m_{04} = 1.04 \times 10^{-4}$ ,  $E^* = 1.14 \times 10^5$  N/mm<sup>2</sup>,  $Y = 2070$  N/mm<sup>2</sup>,  $K = 1.62$ ,  $\psi = 0.5$ ,  $c_h = 0.967$ ,  $\omega_p/\omega_c = 45$ .)

orientation on friction between rough surfaces show that the friction magnitude may change by up to 30% depending on the orientation for rough surfaces and more than 100% for composites, whereas its direction may differ from the sliding direction by an angle of up to a few degrees. However, it is important to consider the directional tendency of dry friction in relation to sliding displacements because it may significantly change the nature of the phenomenon. Taking account of the frictional anisotropy in contact problem leads to a more realistic assessment of these physical processes. There have been many experimental studies devoted to the study of anisotropic friction [67–69]. Special reference should be made to the work carried out by Maksak [67], who investigated the influence of direction of the shear forces on the values of micro-displacements and friction coefficients for machined metallic surfaces. The friction coefficients were shown to be smaller if the machining marks were parallel to sliding direction, as opposed to when they were perpendicular. The differences in the friction coefficients in the range of 10% to 50% were observed. They were strongly dependent on the material of the samples and precision of the machining process. Micro-displacements were more sensitive than the friction coefficients; for the same measurement conditions, the differences of 50–80% were found.

A mathematical description of anisotropic friction has been given first by Huber [70] and later by Michałowski and Mróz [71], Zmitrowicz [72–74], Felder [75], Ho and Curnier [76], Hohberg [77], Mróz and Stupkiewicz [78], Konyukhov and Schweizerhof [79, 80], Konyukhov, Vielsack and Schweizerhof [81] and Hjjaj *et al.* [82]. A numerically treatable theory of orthotropic Coulomb friction has been proposed by Klarbring [83] (an elliptic friction conditions approximated by polygons), Alart [84], Park and Kwak [85], Barbero *et al.* [86] (an elliptic form of friction), Jones and Papadopoulos [87] and Konyukhov and Schweizerhof [88]. Jing *et al.* [89] have developed a 3D-anisotropic

friction model with hardening applied to rock joints and implemented it into a three-dimensional ‘distinct element’ code (DEC). This joint model is based on experimental results from a laboratory investigation on anisotropy and stress dependency of the shear strength and shear deformability of rough joints. A FEM approach based on a hardening friction law and taking into account physical features of the surfaces appears unavailable at present.

The friction law proposed by Fredriksson [90] describes in fact isotropic properties of the interacting surfaces and does not account for anisotropic character of friction phenomena. Therefore, our attempt in the following is made towards constructing a more general frictional model involving the directional coefficient of friction  $\mu_\alpha(\mu_x, \mu_y)$  due to Michałowski and Mróz [71] with the axial friction coefficients  $\mu_x$  and  $\mu_y$  being nonlinear functions of the axial plastic displacements as suggested in [90]. Introducing three independent axial parameters: macroscopic coefficient of friction  $\mu_m$ , slip hardening parameters  $n$  and the initial coefficients of friction  $\mu_o$ , the following relationships may be written

$$\frac{\mu_x}{\mu_{m_x}} = 1 - (1 - \mu_{o_x}) \exp(-n_x u_{T_x}^p), \tag{89}$$

$$\frac{\mu_y}{\mu_{m_y}} = 1 - (1 - \mu_{o_y}) \exp(-n_y u_{T_y}^p). \tag{90}$$

Here,  $\mu_{m_x}$  and  $\mu_{m_y}$  are macroscopic (or static) coefficients of friction,  $\mu_{o_x}$  and  $\mu_{o_y}$  define initial values of  $\mu_{m_x}$  and  $\mu_{m_y}$ , respectively,  $n_x, n_y$  are slip hardening parameters, while  $u_{T_x}^p, u_{T_y}^p$  are the plastic displacements in the  $x$ - and  $y$ -direction, respectively.

A phenomenological description of the frictional phenomena is based here on a similarity of friction and elasto-plastic behaviour. The main features of this model are: (i) decomposition of the contact displacements into an elastic part (describing the preliminary micro-slip or sticking) and a plastic part (describing the macro-slip or sliding), (ii) introduction of a slip function (slip criterion) and a slip potential (analogous to yield function and yield potential in the classical theory of plasticity), (iii) using of a non-associated slip rule for the contact of metallic bodies (non-dilatancy effect), (iv) inclusion of contact compliance (stiffness) parameters due to normal and tangential contact deformation, respectively.

The basic characteristics of the contact model is the form of its sliding function  $f$ , which is specified in terms of contact tractions  $\mathbf{t}_T = (t_x, t_y)$  and contact pressure  $t_N$ . The normal traction component is given by  $\mathbf{t}_N = (\mathbf{n} \otimes \mathbf{n})\mathbf{t} = (\mathbf{t}\mathbf{n})\mathbf{n} = t_N \mathbf{n}$ , while the tangential one by  $\mathbf{t}_T = (\mathbf{I} - \mathbf{n} \otimes \mathbf{n})\mathbf{t} = \mathbf{t} - t_N \mathbf{n}$ , where  $\mathbf{n}$  denotes the unit vector normal to the contact surface and  $\otimes$  is the tensor product of two vectors.

Let us approximate the limit friction condition by an ellipse with its axes coinciding with the orthotropy axes [71, 78]

$$f(t_x, t_y, t_N) = \left[ \left( \frac{t_x}{\mu_x} \right)^2 + \left( \frac{t_y}{\mu_y} \right)^2 \right]^{\frac{1}{2}} - t_N = 0, \tag{91}$$

where  $\mu_x$  and  $\mu_y$  are the principal friction coefficients along the orthotropy axes  $x$  and  $y$ , defined by (89) and (90).

The following additive relation is assumed for the incremental elasto-plastic sliding model

$$\Delta \mathbf{u} = (\Delta \mathbf{u}_T^e + \Delta \mathbf{u}_T^p) + (\Delta \mathbf{u}_N^e + \Delta \mathbf{u}_N^p) \mathbf{n} \tag{92}$$

with the contact displacements indexed by  $e$  and  $p$  corresponding to the elastic (reversible) and plastic (irreversible) behaviour, respectively. The elastic constitutive incremental relationship may be written as

$$\Delta \mathbf{t} = \mathbf{D}_c^e \Delta \mathbf{u}^e \tag{93}$$

with

$$\mathbf{D}_c^e = \begin{bmatrix} k_{T_x} & 0 & 0 \\ 0 & k_{T_y} & 0 \\ 0 & 0 & k_N \end{bmatrix}, \tag{94}$$

where  $k_{T_x}, k_{T_y}$  are the tangential elastic stiffness coefficients in the  $x$ - and  $y$ -direction, respectively, and  $k_N$  is the normal stiffness parameter.

Test results have demonstrated that the shear stiffness parameters  $k_{T_x}$  and  $k_{T_y}$  are generally different. The elastic or elasto-plastic normal stiffness coefficients per unit area can be found from the analysis of Sects. 4 and 7. The elastic normal stiffness per unit area (cf. (55)) is given by

$$k_N = 2D_{sum} E^* (m_{00} \mu)^{1/4} \times \int_l^\infty \int_0^\infty \int_0^\infty f_2(e) (\omega_1 - l)^{1/2} (1/\kappa_m)^{1/2} \times p_{sum}(\omega_6, \omega_4, \omega_1) d\omega_6 d\omega_4 d\omega_1. \tag{95}$$

The interesting features of the ratio of the initial tangential to the normal stiffness is found by Mindlin [91] as a linear combination of complete elliptic integrals. In the case in which the two bodies have the same elastic properties the initials tangential stiffnesses in the direction of the major and minor axes of the ellipse  $x$ - and  $y$ -direction, respectively, are

$$\frac{k_N}{k_T} = \begin{cases} \frac{\pi(2-\nu)}{4(1-\nu)} \frac{1}{K(e)} \frac{2K(e)}{\pi} - \frac{\nu}{2\pi^2(2-\nu)} \frac{N(e)}{e}, \\ \quad B < A \text{ (minor axis) } (k_T = k_{T_y}), \\ \frac{\pi(2-\nu)}{4(1-\nu)} \frac{1}{K_1(k_1)} \frac{2K_1(k_1)}{\pi} - \frac{\nu}{2\pi^2(2-\nu)} \frac{N_1(k_1)}{k_1}, \\ \quad B > A \text{ (major axis) } (k_T = k_{T_x}), \end{cases} \tag{96}$$

**Table 3** Ratio of  $k_N/k_T$  of bodies with the same elastic constants

$B^2/A^2$	$\nu = 0.0$	$\nu = 1/4$	$\nu = 1/2$
10.E-03	1.0	1.06874	1.20622
10.E-02	1.0	1.08920	1.26759
10.E-01	1.0	1.12167	1.36502
10.E-00	1.0	1.16667	1.5
10.E+01	1.0	1.21166	1.63497
10.E+02	1.0	1.24413	1.73241
10.E+03	1.0	1.26459	1.79378

where  $K(e)$  is complete elliptic integrals of the first kind and quantity  $N(e)$  is combination of the elliptic integrals of argument  $e$ ;  $K_1(k_1)$  and  $N_1(k_1)$  are similar integrals of argument  $k_1^2 = 1 - A^2/B^2 = 1 - 1/(1 - e^2)$ .

Due to Mindlin [91], the quantity  $N(e)$  is

$$N(e) = 4\pi \left[ \left( \frac{2}{e} - e \right) K(e) - \frac{2}{e} E(e) \right]. \tag{97}$$

The ratio of normal stiffness  $k_N$  to initial tangential stiffness  $k_T$  of bodies with like elastic material constants, computed from (96) can be taken from Table 3. It may be seen that tangential stiffness increases as the Poisson’s ratio decreases and the stiffness in the direction of the major axis is smaller than the stiffness in the direction of minor axis. When  $\nu = 0.$ , the tangential stiffness is isotropic, over the range  $0. < \nu < 0.5$  the normal stiffness is always greater than the initial tangential stiffness, but never more than twice. Several limiting cases of results from numerical calculations are as follows: (i) for  $\nu = 0$ ,  $k_N/k_T = 1.$ , (ii)  $B/A \rightarrow 0$ ,  $k_N/k_T = 1.$ , (iii)  $B/A \rightarrow \infty$ ,  $k_N/k_T = 1/(1 - \nu)$ , (iv)  $B/A = 1.$ ,  $k_N/k_T = [(2 - \nu)/2(1 - \nu)]$ .

The model presented involves both the friction condition (see (91)) and the sliding rule. The sliding rule can be generated by adopting a non-associated interface convex slip potential (for the known contact pressure represented by an ellipse) written as in [78]

$$g(t_x, t_y, t_N) = \left[ \left( \frac{t_x}{\nu_x} \right)^2 + \left( \frac{t_y}{\nu_y} \right)^2 \right]^{\frac{1}{2}} - t_N = 0, \tag{98}$$

$$\frac{\nu_y}{\nu_x} = \left( \frac{\mu_y}{\mu_x} \right)^k.$$

The plastic (irreversible) part of the contact displacement increment with the above sliding rule is written as

$$\Delta \mathbf{u}^p = \gamma \frac{\partial g}{\partial \mathbf{t}}, \tag{99}$$

where the plastic/slip potential gradient gives the direction of the slip,  $\gamma$  denotes a non-negative plastic/slip multiplier

defined as

$$\begin{aligned} \gamma &= 0 \quad \text{for } f < 0 \text{ or } f = 0 \quad \text{and} \\ \Delta f &= \frac{\partial f}{\partial \mathbf{t}} \Delta \mathbf{t} + \frac{\partial f}{\partial \mathbf{u}_T^p} \Delta \mathbf{u}_T^p < 0, \\ \gamma &\geq 0 \quad \text{for } f = 0 \quad \text{and} \\ \Delta f &= \frac{\partial f}{\partial \mathbf{t}} \Delta \mathbf{t} + \frac{\partial f}{\partial \mathbf{u}_T^p} \Delta \mathbf{u}_T^p = 0 \end{aligned} \tag{100}$$

$\nu_x$  and  $\nu_y$  are the principal axes ratio of sliding potential along the orthotropy axes and  $k$  specifies the shape of the slip potential. For  $k = 1$  we have the associated sliding rule,  $f = g$ ; for  $k = 0$  the slip potential is a circle implying a sliding velocity coaxial with the friction force ( $\alpha = \beta$ ). The deviation angle ( $\alpha - \beta$ ) which characterises the anisotropic friction is equal to the angle between the friction force  $\mathbf{t}_T = \mathbf{t}_T(t_x, t_y)$  and the increment of the sliding displacement vector  $\Delta \mathbf{u}_T^p = \Delta \mathbf{u}_T^p(\Delta u_x^p, \Delta u_y^p)$ , cf. Fig. 9. Adopting the associated slip law in which  $f = g$  would yield as a rule a non-zero value for the uplifting normal incremental plastic displacement  $u_N^p$  (dilatancy phenomena). Since such a behaviour for metallic bodies finds no experimental support, a non-associated slip law should be adopted in which  $f \neq g$ . (The dilatancy problem plays a fundamental role in geomechanics; for further information we refer the reader to References [69, 77, 89, 94, 95].) The non-associated slip rule is considered in the following investigation by setting  $\Delta u_N^p = 0$ . For the special case of the non-associated friction in which the slip potential  $g$  will be assumed in the form of the Huber-von Mises cylinder (the direction of sliding is contact pressure independent so that no dilatancy effect is generated), the slip potential  $g$  is modified as follows

$$g(t_x, t_y, t_N) = \left[ \left( \frac{t_x}{\nu_x} \right)^2 + \left( \frac{t_y}{\nu_y} \right)^2 \right]^{\frac{1}{2}} - C \tag{101}$$

with  $C$  being a constant value.

For sticking and unloading (i.e.  $f < 0$ ) we apply the incremental form of (93). If  $f = 0$  there exist two possibilities: continuing sliding and ‘unloading’ sticking. For ‘plasticity’ along the continuing sliding path, it follows from (93), (99) and (100) that

$$\frac{\partial f}{\partial \mathbf{t}} \left[ \mathbf{D}_c^e \left( \Delta \mathbf{u} - \gamma \frac{\partial g}{\partial \mathbf{t}} \right) \right] + \frac{\partial f}{\partial \mathbf{u}_T^p} \gamma \frac{\partial g}{\partial \mathbf{t}_T} = 0. \tag{102}$$

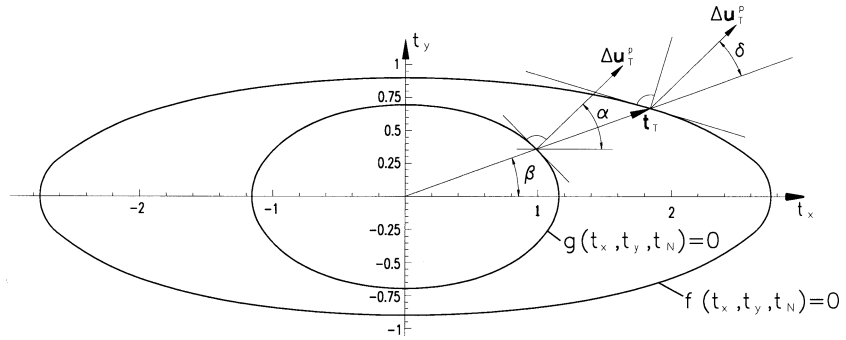
After some mathematical manipulations the plastic/slip scalar  $\gamma$  in (99) is computed as

$$\gamma = \left[ \frac{\partial f}{\partial \mathbf{t}} \left( \mathbf{D}_c^e \Delta \mathbf{u} \right) \right] \left[ \frac{\partial f}{\partial \mathbf{t}} \left( \mathbf{D}_c^e \frac{\partial g}{\partial \mathbf{t}} \right) - \frac{\partial f}{\partial \mathbf{u}_T^p} \frac{\partial g}{\partial \mathbf{t}_T} \right]^{-1}. \tag{103}$$

On account of (92), (99) and (103) we arrive at the following incremental constitutive relation:

$$\Delta \mathbf{t} = \mathbf{D}_c^{ep} \Delta \mathbf{u} \tag{104}$$

**Fig. 9** Friction and sliding rules generated by limit friction surface  $f(t_x, t_y, t_N)$  and sliding potential  $g(t_x, t_y, t_N)$



with

$$\mathbf{D}_c^{ep} = \mathbf{D}_c^e - \mathbf{D}_c^e \frac{\partial g}{\partial \mathbf{t}} \otimes \mathbf{D}_c^e \frac{\partial f}{\partial \mathbf{t}} \left[ \frac{\partial f}{\partial \mathbf{t}} \left( \mathbf{D}_c^e \frac{\partial g}{\partial \mathbf{t}} \right) - H \right]^{-1}. \quad (105)$$

By using (91) and (101) and employing the notation

$$\begin{aligned} c_x &= \frac{\partial f}{\partial t_x} = \frac{t_x}{\mu_x^2 \left[ \left( \frac{t_x}{\mu_x} \right)^2 + \left( \frac{t_y}{\mu_y} \right)^2 \right]^{\frac{1}{2}}}, \\ c_y &= \frac{\partial f}{\partial t_y} = \frac{t_y}{\mu_y^2 \left[ \left( \frac{t_x}{\mu_x} \right)^2 + \left( \frac{t_y}{\mu_y} \right)^2 \right]^{\frac{1}{2}}}, \\ c_z &= \frac{\partial f}{\partial t_N} = -1, \end{aligned} \quad (106)$$

$$\begin{aligned} d_x &= \frac{\partial g}{\partial t_x} = \frac{t_x}{v_x^2 \left[ \left( \frac{t_x}{v_x} \right)^2 + \left( \frac{t_y}{v_y} \right)^2 \right]^{\frac{1}{2}}}, \\ d_y &= \frac{\partial g}{\partial t_y} = \frac{t_y}{v_y^2 \left[ \left( \frac{t_x}{v_x} \right)^2 + \left( \frac{t_y}{v_y} \right)^2 \right]^{\frac{1}{2}}}, \\ d_z &= \frac{\partial g}{\partial t_N} = 0 \end{aligned}$$

the 3D-constitutive interface matrix  $\mathbf{D}_c^{ep}$  (for the elastic case  $\mathbf{D}_c^{ep}$  equals  $\mathbf{D}_c^e$  from (94)) can be expressed more explicitly as

$$\mathbf{D}_c^{ep} = \frac{1}{A - H} \begin{bmatrix} k_{T_x}(k_N c_z d_z + k_{T_y} c_y d_y - H) & -k_{T_x} k_{T_y} c_y d_x & -k_{T_x} k_N c_z d_x \\ -k_{T_x} k_{T_y} c_x d_y & k_{T_y}(k_{T_x} c_x d_x + k_N c_z d_z - H) & -k_{T_y} k_N c_z d_y \\ -k_{T_x} k_N c_x d_z & -k_{T_y} k_N c_y d_z & k_N(k_{T_x} c_x d_x + k_{T_y} c_y d_y - H) \end{bmatrix}, \quad (107)$$

where

$$A = k_{T_x} c_x d_x + k_{T_y} c_y d_y + k_N c_z d_z \quad (108)$$

and  $H$  is a friction hardening parameter expressed as

$$H = \frac{\partial f}{\partial \mathbf{u}_T^p} \frac{\partial g}{\partial \mathbf{t}_T} = \frac{\partial f}{\partial \mu_x} \frac{\partial \mu_x}{\partial u_{T_x}^p} \frac{\partial g}{\partial t_x} + \frac{\partial f}{\partial \mu_y} \frac{\partial \mu_y}{\partial u_{T_y}^p} \frac{\partial g}{\partial t_y} \quad (109)$$

or, more explicitly, as

$$H = - \left[ \frac{t_x^2 \frac{\partial \mu_x}{\partial u_{T_x}^p} d_x}{\mu_x^3 \sqrt{\left( \frac{t_x}{\mu_x} \right)^2 + \left( \frac{t_y}{\mu_y} \right)^2}} + \frac{t_y^2 \frac{\partial \mu_y}{\partial u_{T_y}^p} d_y}{\mu_y^3 \sqrt{\left( \frac{t_x}{\mu_x} \right)^2 + \left( \frac{t_y}{\mu_y} \right)^2}} \right]. \quad (110)$$

In general, the coefficients of friction are not constant and may depend upon the plastic relative contact displacements and the partial derivative of the normalised coefficients of

friction with respect the plastic (irreversible) displacements as, (cf. (89) and (90))

$$\frac{\partial \mu_x}{\partial u_{T_x}^p} = n_x \mu_{m_x} (1 - \mu_{o_x}) \exp(-n_x u_{T_x}^p) \quad (111)$$

and

$$\frac{\partial \mu_y}{\partial u_{T_y}^p} = n_y \mu_{m_y} (1 - \mu_{o_y}) \exp(-n_y u_{T_y}^p). \quad (112)$$

If there were no hardening or softening effects for the sliding motion, the axial friction coefficients would be constant during the entire process, i.e. the value of the hardening parameter  $H$  determined by (110) would be zero. For the increment of the tangential displacement  $\Delta \mathbf{u}_T^p$ , it follows from (99) and (103) that

$$\Delta \mathbf{u}_T^p = \left[ \frac{\partial f}{\partial \mathbf{t}} \left( \mathbf{D}_c^e \frac{\partial g}{\partial \mathbf{t}} \right) - H \right]^{-1} \left[ \frac{\partial f}{\partial \mathbf{t}} \left( \mathbf{D}_c^e \Delta \mathbf{u} \right) \right] \frac{\partial g}{\partial \mathbf{t}_T}. \quad (113)$$

Denoting the inclination angle of the incremental plastic (or sliding) displacement  $\Delta \mathbf{u}_T^p$  with respect to the  $x$ -axis (see Fig. 12) by  $\alpha$ , we have

$$\tan \alpha = \frac{\Delta u_{Ty}^p}{\Delta u_{Tx}^p}. \tag{114}$$

The loading is applied in increments; at each load increment we compute the contact traction  $\mathbf{t}_T$ . If the tangential traction at the end of an increment is larger than the critical value a correction has to be made because the tangential traction can at most be equal to  $(t_N \mu_\alpha)$ . A value  $\mu_\alpha$  defines the effective (or directional) coefficient of friction in the direction which has an inclination angle  $\alpha$  with respect to the  $x$ -axis. The coefficient  $\mu_\alpha$  may be expressed in terms of the inclination angle  $\alpha$  as in [71]

$$\mu_\alpha = \sqrt{\frac{\mu_x^4 \cos^2 \alpha + \mu_y^4 \sin^2 \alpha}{\mu_x^2 \cos^2 \alpha + \mu_y^2 \sin^2 \alpha}}, \tag{115}$$

where  $\mu_x$  and  $\mu_y$  are the principal friction functions along the axes  $x$  and  $y$  defined by (89) and (90). With the help of the so defined inclination angle  $\alpha$ , the limited (when sliding occurs) traction components  $t_x$  and  $t_y$  are then given by

$$t_x = t_N \mu_\alpha \cos \beta, \quad t_y = t_N \mu_\alpha \sin \beta, \tag{116}$$

where  $t_N$  is the normal traction at the end of iteration ( $i$ ) calculated as

$$t_N^{(i)} = t_N^{(i-1)} + k_N \Delta u_N^{(i)}, \tag{117}$$

where  $\Delta u_N^{(i)}$  denotes the  $i$ -th incremental change in the relative normal approach and  $k_N$  is the normal stiffness parameter defined in (95).

From (106)<sub>4</sub>, (106)<sub>5</sub>, (114) and (116) the relation between  $\alpha$  and  $\beta$  takes the form

$$\tan \beta = \tan \alpha \left( \frac{v_y}{v_x} \right)^2, \tag{118}$$

where  $v_x$  and  $v_y$  are the principal ellipse axes determined by the sliding potential along the orthotropy axes  $x$  and  $y$ , respectively (cf. (101)). It is seen from (118) that the slip in the direction of  $\Delta \mathbf{u}_T^p$  is not generally collinear with the limited friction traction vector  $\mathbf{t}_T$ . In the case of an isotropic slip criterion with the  $\mu_x = \mu_y$ , the angles  $\alpha$  and  $\beta$  are equal,

i.e. the deviation angle  $(\alpha - \beta)$  becomes zero, (see Fig. 12) and the contact matrix  $\mathbf{D}_c^{ep}$  given in [92, 93] is recovered. For an orthotropic non-hardening friction model ( $\mu_x, \mu_y = \text{const.}$ ) we refer the reader to [77].

### 8.2 Isotropic Hardening Model

The model presented involves three independent axial parameters: macroscopic coefficient of friction  $\mu_m$ , slip hardening parameters  $n$  and the initial coefficients of friction  $\beta$ . After Fredriksson [90] the following relationships may be written

$$\frac{\mu_F}{\mu_m} = 1 - (1 - \beta) \exp(-n \|\mathbf{u}_T^p\|). \tag{119}$$

Here,  $\mu_m$  is macroscopic (or static) coefficient of friction,  $\beta$  defines initial value of  $\mu_m$ ,  $n$  is slip hardening parameter and  $\|\mathbf{u}_T^p\| = u_{T_{eff}}^p$  is the effective plastic displacement.

Let us approximate the limit friction condition by a paraboloid slip surface

$$f(t_x, t_y, t_N) = (t_x^2 + t_y^2)^{\frac{1}{2}} - \mu_F t_N = 0, \tag{120}$$

where  $\mu_F$  is the friction coefficient defined by (119).

The slip potential  $g$  is assumed as follows:

$$g(t_x, t_y, t_N) = (t_x^2 + t_y^2)^{\frac{1}{2}} - C = 0, \tag{121}$$

with  $C$  being a constant value.

By employing the following notation:

$$\begin{aligned} c_x &= \frac{\partial f}{\partial t_x} = \frac{t_x}{(t_x^2 + t_y^2)^{\frac{1}{2}}}, \\ c_y &= \frac{\partial f}{\partial t_y} = \frac{t_y}{(t_x^2 + t_y^2)^{\frac{1}{2}}}, \\ c_z &= \frac{\partial f}{\partial t_N} = -\mu_F, \\ d_x &= \frac{\partial g}{\partial t_x} = \frac{t_x}{(t_x^2 + t_y^2)^{\frac{1}{2}}}, \\ d_y &= \frac{\partial g}{\partial t_y} = \frac{t_y}{(t_x^2 + t_y^2)^{\frac{1}{2}}}, \\ d_z &= \frac{\partial g}{\partial t_N} = 0, \end{aligned} \tag{122}$$

the 3D-constitutive interface matrix  $\mathbf{D}_c^{ep}$  can be expressed as

$$\mathbf{D}_c^{ep} = \frac{1}{A - H} \begin{bmatrix} k_{T_x}(k_N c_z d_z + k_{T_y} c_y d_y - H) & -k_{T_x} k_{T_y} c_y d_x & -k_{T_x} k_N c_z d_x \\ -k_{T_x} k_{T_y} c_x d_y & k_{T_y}(k_{T_x} c_x d_x + k_N c_z d_z - H) & -k_{T_y} k_N c_z d_y \\ -k_{T_x} k_N c_x d_z & -k_{T_y} k_N c_y d_z & k_N(k_{T_x} c_x d_x + k_{T_y} c_y d_y - H) \end{bmatrix}, \tag{123}$$

where

$$A = k_{T_x}c_x d_x + k_{T_y}c_y d_y + k_N c_z d_z, \tag{124}$$

and  $H$  is a friction hardening parameter expressed as

$$H = \frac{\partial f}{\partial \mathbf{u}_T^p} \frac{\partial g}{\partial \mathbf{t}_T} = \frac{\partial f}{\partial \mu_F} \frac{\partial \mu_F}{\partial u_{T_x}^p} \frac{\partial g}{\partial t_x} + \frac{\partial f}{\partial \mu_F} \frac{\partial \mu_F}{\partial u_{T_y}^p} \frac{\partial g}{\partial t_y}, \tag{125}$$

or, more explicitly

$$H = t_N \frac{\partial \mu_F}{\partial u_{T_{eff}}^p} \left( \frac{k_{T_x} \cos \alpha + k_{T_y} \tan \alpha \sin \alpha}{\sqrt{k_{T_y}^2 \tan^2 \alpha + k_{T_x}^2}} \right), \tag{126}$$

while the inclination angle between the plastic (or sliding) displacement vector  $\mathbf{u}_T^p$  and the  $x$ -axis denoted by  $\alpha$ , is determined as

$$\tan \alpha = \frac{\Delta u_{T_y}^p}{\Delta u_{T_x}^p}. \tag{127}$$

For the increment of the tangential displacement  $\Delta \mathbf{u}_T^p$ , it follows (Sect. 8.1) that

$$\Delta \mathbf{u}_T^p = \left[ \frac{\partial f}{\partial \mathbf{t}} \left( \mathbf{D}_c^e \frac{\partial g}{\partial \mathbf{t}} \right) - H \right]^{-1} \left[ \frac{\partial f}{\partial \mathbf{t}} \left( \mathbf{D}_c^e \Delta \mathbf{u} \right) \right] \frac{\partial g}{\partial \mathbf{t}}. \tag{128}$$

In this model the coefficient of friction is not constant and may depend upon the effective plastic displacement (see (119)); then the partial derivative of the normalised coefficients of friction with respect to the plastic (irreversible) displacements gives

$$\frac{\partial \mu_F}{\partial u_{T_{eff}}^p} = n \mu_m (1 - \beta) \exp(-n u_{T_{eff}}^p). \tag{129}$$

If there were no hardening effects for the sliding motion, the friction coefficients would be constant during the entire

process, i.e. the value of the hardening parameter  $H$  determined by (125) would be zero.

The inclination angle between the vector of the traction  $\mathbf{t}_T$  and the  $x$ -axis denoted by  $\beta$ , can be defined then (Sect. 8.1; the anisotropic friction criterion transforms into an isotropic one in which the  $(t_x, t_y)$ -plane is represented by the circle) as

$$\tan \beta = \frac{t_{T_y}}{t_{T_x}} = \tan \alpha. \tag{130}$$

Note that due to anisotropic properties of the contact surface the values of angles  $\alpha$  and  $\beta$  are different. If  $k_{T_x}$  equals  $k_{T_y}$  (isotropic properties of the contact surface) then (126) reduces to

$$H = t_N \frac{\partial \mu_F}{\partial u_{T_{eff}}^p}. \tag{131}$$

The present formulation is believed to provide with some further insight into the problem by accounting for a more general sliding model for the contact interface reaching its critical state for friction models for low contact pressure, up to 10 MPa. The model presented, however, is not valid for behaviour at contact surfaces which are characterised by high contact pressures, bulk plastic deformation, high temperatures of one or both contacting bodies. The most common approaches of describing the frictional effect between tools and workpiece can be given by the normal pressure-dependent model, micro-mechanical models accounting for asperity deformation or phenomenological models based on the theory for steady-state frictional wear effects; see a review study given by Black *et al.* [96]. Recently, Mróz and Stupkiewicz [97] have presented a combined friction model affecting irreversible asperity flattening, plugging as well as adhesion occurring at the workpiece-tool interface in metal-forming processes.

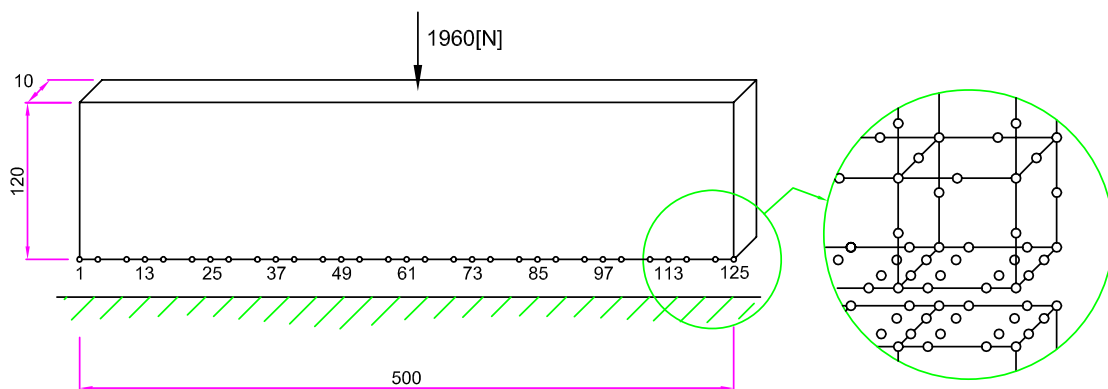


Fig. 10 Elastic beam on rigid base

### 9 Numerical Example

#### 9.1 Prismatic Beam on Rigid Base (Fig. 10)

An elastic beam of rectangular cross-section of  $10 \times 120$  mm and length of 500 mm lying with one of its longitudinal narrow faces against a flat rigid base (Fig. 10) is chosen as numerical example. A total external load compressing the prism against the rigid base was applied at the prism mid-length and had the magnitude of 1962 N. The initial load was chosen as 4.9 N. The harmonic elastic modulus  $E^*$  of  $1.127 \times 10^5$  MPa (see (42)) that corresponds to the modulus of elasticity of the beam  $E_1 = 1.057 \times 10^5$  MPa

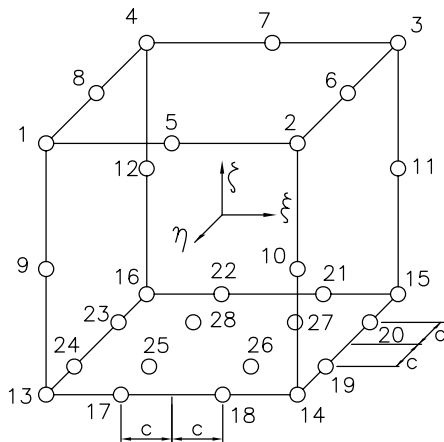


Fig. 11 28-node hexahedral transition element;  $c = 1/\sqrt{5}$

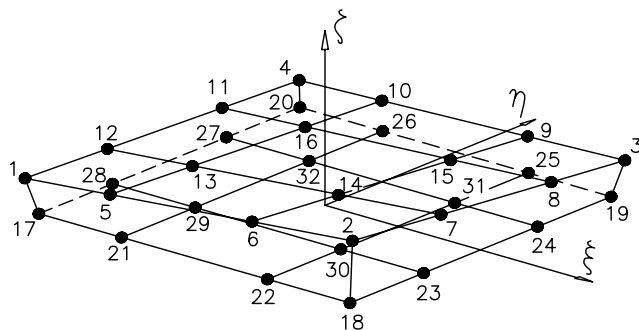
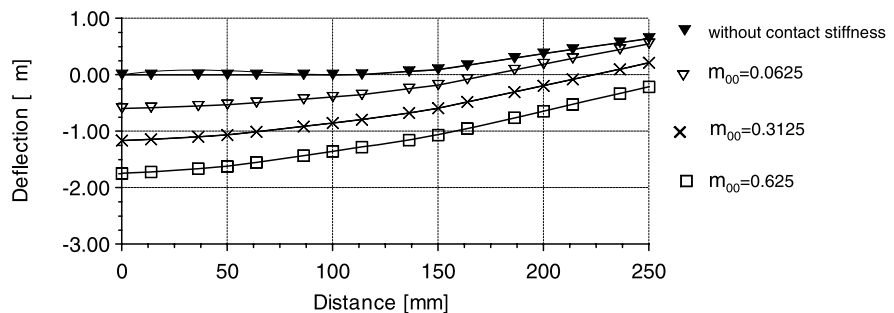


Fig. 12 32-node cubic interface element of zero-thickness

Fig. 13 Interface deflections for a beam on a rigid base for different values of variances of surface height:  $m_{00} = 0.0625$  (triangles),  $m_{00} = 0.3125$  (crosses),  $m_{00} = 0.625$  (squares); ( $m_{20} = 8. \times 10^{-5}$ ,  $m_{02} = 8. \times 10^{-4}$ ,  $m_{40} = 1.04 \times 10^{-6}$ ,  $m_{04} = 1.04 \times 10^{-4}$ )

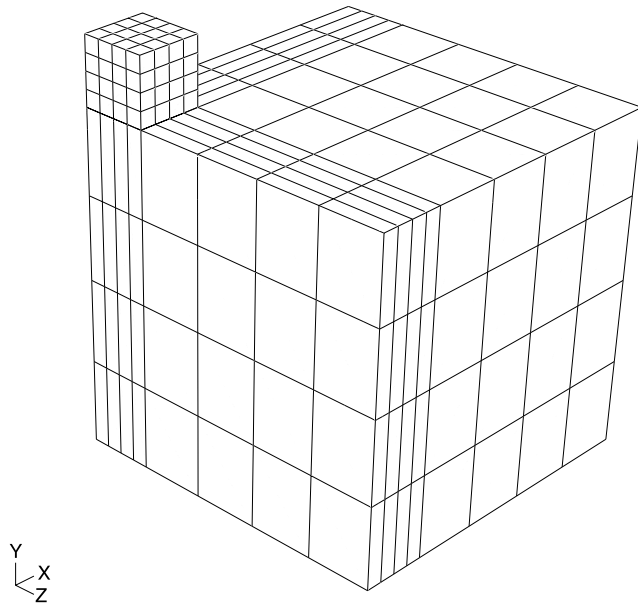


and Poisson ratio of  $\nu_1 = 0.25$  was taken. (If one of contacting surfaces is much more elastic than the other, therefore  $E^* = E_1/(1 - \nu_1^2)$  is just the plane-strain modulus.) The numerical result is presented for a case in which the Young modulus of the foundation is  $10^5$  times larger than that of the beam; in effect, a rigid base is considered.

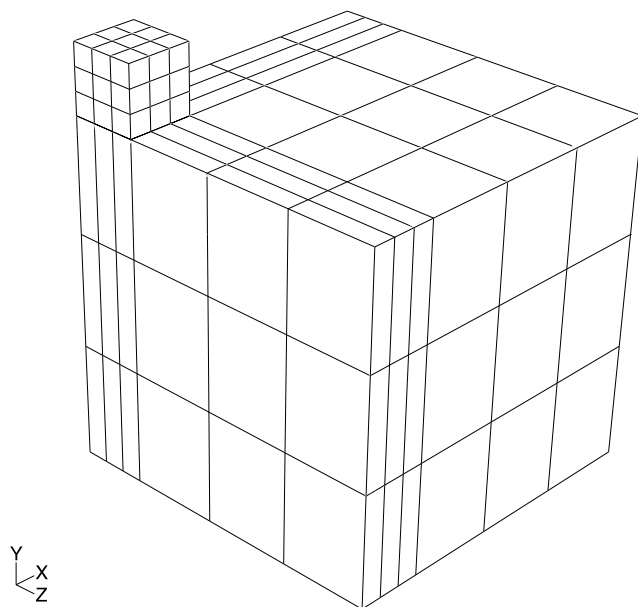
Except for the contact zone the beam was discretized by 20-noded hexahedral elements connected with the 28-noded hexahedral transition elements (see Fig. 11) in the neighbourhood of the contact zone. The contact zone is discretized by the 32-node cubic interface element of zero-thickness as shown in Fig. 12. Since the model is symmetric, suitable boundary constraints were imposed on nodes situated on the centre-line and only half of the structure is analysed. The contact constraints are introduced by the penalty technique combined with an active search strategy. This problem was analysed by using sixteen load increments. For finite element calculations the coefficients of the normal and tangential contact stiffness obtained according to formulae (95) and (96), respectively, were taken. For comparison results using the elastic and elasto-plastic normal contact stiffnesses are given in Table 4. The maximum surface deflections occur in the middle of the beam and these values strongly depend on the values of  $m_{00}$  (see Fig. 13; these results are given for elastic model). There is no systematic difference between the results obtained by the elastic and elasto-plastic models. It was found that in several cases

Table 4 Contact deflection values at the central,  $u_{N_{max}}$ , and at end of the beam,  $u_{N_{min}}$ ;  $m_{20} = 8. \times 10^{-5}$ ,  $m_{02} = 8. \times 10^{-4}$ ,  $m_{40} = 1.04 \times 10^{-6}$ ,  $m_{04} = 1.04 \times 10^{-4}$ ,  $E^* = 1.14 \times 10^5$  N/mm<sup>2</sup>,  $Y = 2070$  N/mm<sup>2</sup>,  $K = 1.62$ ,  $\psi = 0.35$ ,  $c_h = 0.967\omega_p/\omega_c = 45$

The case	$u_{N_{max}}$ , $\mu\text{m}$	$u_{N_{min}}$ , $\mu\text{m}$
1. $m_{00} = 0.6250$ (elastic)	-1.261	+0.153
2. $m_{00} = 0.3125$ (elastic)	-1.023	+0.316
3. $m_{00} = 0.0625$ (elastic)	-0.577	+0.556
4. $m_{00} = 0.6250$ (elasto-plastic)	-1.744	-0.212
5. $m_{00} = 0.3125$ (elasto-plastic)	-1.162	+0.214
6. $m_{00} = 0.0625$ (elasto-plastic)	-0.595	+0.551



**Fig. 14** Elastic punch on elastic foundation using 21-node transition elements in the contact zone



**Fig. 15** Elastic punch on elastic foundation using 28-node transition elements in the contact zone

**Table 5** The total dissipation energy  $D$  [Nmm]

	case (a)	case (b)	case (c)
21-node	0.2478	0.2540	0.0150
28-node	0.2114	0.1868	0.0162

some nodes at the outer edge of the beam were detected not be in contact (separation occurs).

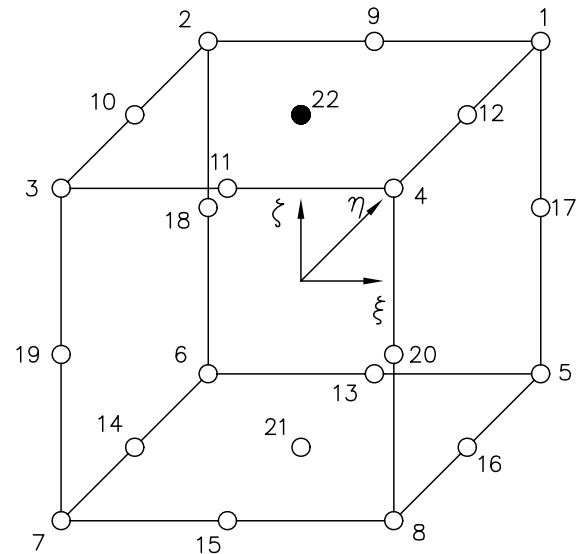


**Fig. 16** 21-node hexahedral transition element

### 9.2 Elastic Flat-Punch on Elastic Foundation (Figs. 14 and 15)

To test an orthotropic effect a flat-ended elastic punch pressed into an elastic foundation is chosen as the next example. The problem of loading and unloading of elastic half-space by a flat square punch, for which the frictional interface conditions prevail, was discussed by Klarbring [83] and Park and Kwak [85]. In both the cases an ideal friction model (no hardening) neglecting microirregularities of contact surface was assumed. Here, a monotonically increasing uniformly distributed load is applied at one 20-noded hexahedral finite element in the middle of the punch. Dimensions of the punch and elastic foundation are  $20 \times 20 \times 10$  mm and  $100 \times 100 \times 50$  mm, respectively. The elasticity modulus for both the bodies equals 200 GPa and the Poisson's ratio is taken to be 0.25. Except for the contact zone the punch and the foundation were discretized by 20-noded connected with the 21-noded transition hexahedral elements (see Fig. 16) in the neighbourhood of the contact zone or with 28-noded hexahedral transition elements as shown in Fig. 11. For the first case, the contact zone was discretized by the 18-node quadratic as shown in Fig. 17 or by the 32 node cubic interface element of zero-thickness (Fig. 12) for the second one. A complete description of the special finite elements used are available in [98] and [99]. Since the model is symmetric, suitable boundary constraints were imposed on nodes situated on the centre-surfaces and only a quarter of the structure was analysed. The contact constraints are introduced by the penalty technique combined with an active search strategy. For the incremental method employed the accuracy obtained depends upon the number of steps. This problem was analysed by using sixteen load increments. Slip hardening parameters of  $n_x = n_y = 275$  1/mm are assumed. The effect

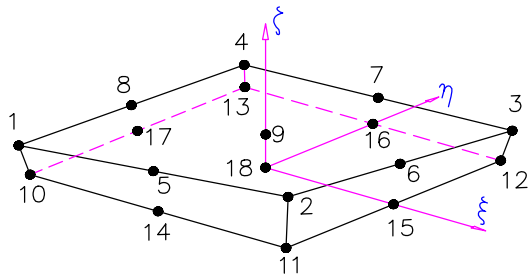


**Fig. 17** 18-node quadratic interface element of zero-thickness

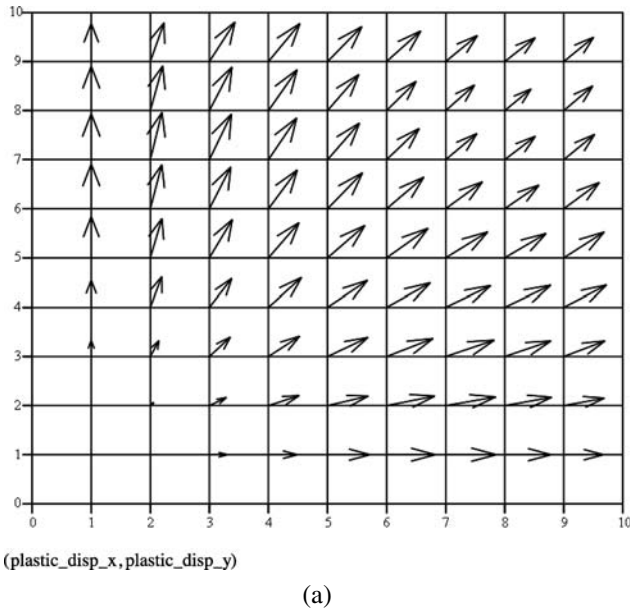
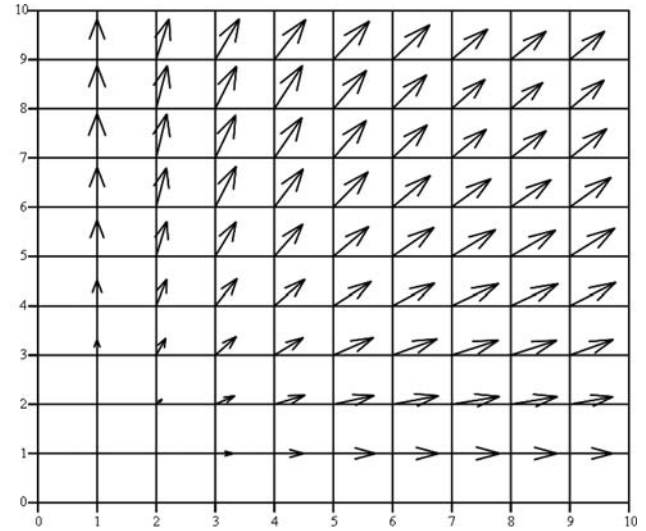


**Fig. 18** Directions of tangential plastic displacements at 81 contact points using 21-node transition elements for different slip models and external load value of 1000 N;  $m_{00} = 0.625$ ,  $m_{20} = 8. \times 10^{-5}$ ,  $m_{02} = 8. \times 10^{-4}$ ,  $m_{40} = 1.04 \times 10^{-6}$ ,  $m_{04} = 1.04 \times 10^{-4}$ ,  $E_1 = E_2 = 2. \times 10^5$  N/mm<sup>2</sup>,  $\nu_1 = \nu_2 = 0.25$ ,  $Y = 2070$  N/mm<sup>2</sup>,  $K = 1.62$ ,  $\psi = 0.35$ ,  $c_h = 0.967\omega_p/\omega_c = 45$ .: (a)  $\mu_{m_x} = \mu_{m_y} = 0.2$ ,  $\mu_{o_x} = \mu_{o_y} = 1.$ ,  $\nu_x = \nu_y = 0.125$ ,  $k_{T_x} = k_{T_y} = 0.7k_n$ , (b)  $\mu_{m_x} = \mu_{m_y} = 0.5$ ,  $\mu_{o_x} = \mu_{o_y} = 0.5$ ,  $\nu_x = \nu_y = 0.125$ ,  $k_{T_x} = k_{T_y} = 0.7k_n$ , (c)  $\mu_{m_x} = \mu_{m_y} = 0.5$ ,  $\mu_{o_x} = \mu_{o_y} = 0.5$ ,  $\nu_x = \nu_y = 0.125$ ,  $k_{T_x} = 0.7k_n$ ,  $k_{T_y} = k_n$

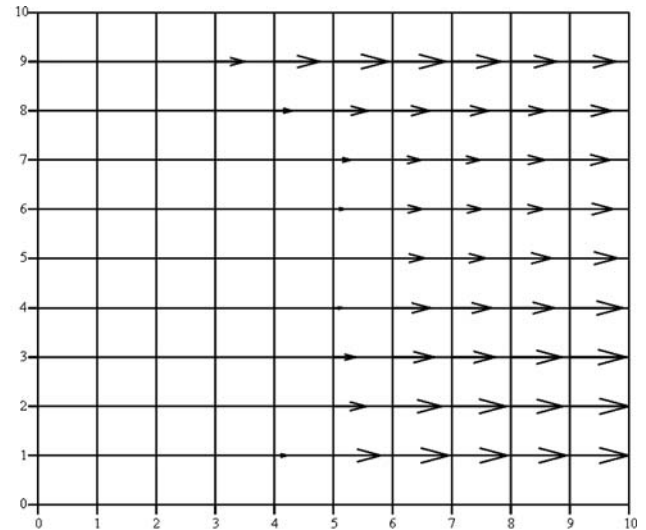
of friction properties on the plastic contact displacements for the different orthotropy models are illustrated on Figs. from 18(a) to 18(c) and 19(a) to 19(c).

By analogy to the corresponding problem of a circular-cylinder [100] we expect to find an adhesion in the centre of the contact surface and a region of slip at the punch edge. This is exactly what has been found in the calculation.

The greatest magnitude of the frictional dissipation energies defined as the scalar product of the tangential forces (traction forces)  $\mathbf{t}_T$  and the plastic displacements  $\mathbf{u}_T^p$ , i.e.  $D = \mathbf{t}_T \mathbf{u}_T^p = t_x u_x^p + t_y u_y^p$ , was obtained for the case of  $\mu_{m_x} = \mu_{m_y} = 0.5$  and  $\mu_{o_x} = \mu_{o_y} = 0.5$  shown in the



(b)

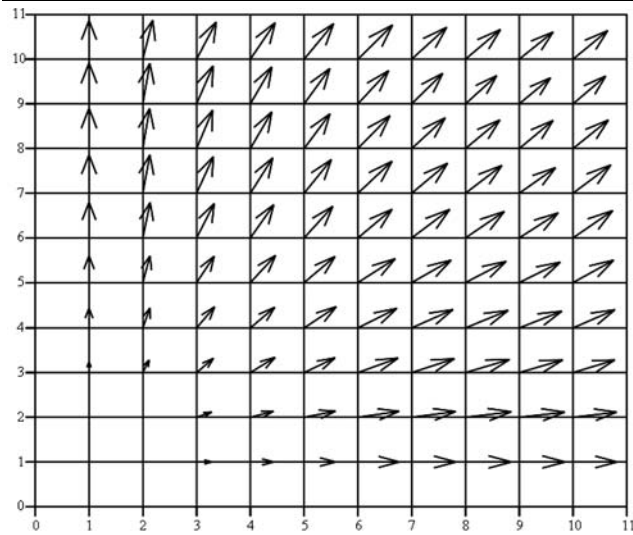


(c)

**Fig. 18** (Continued)

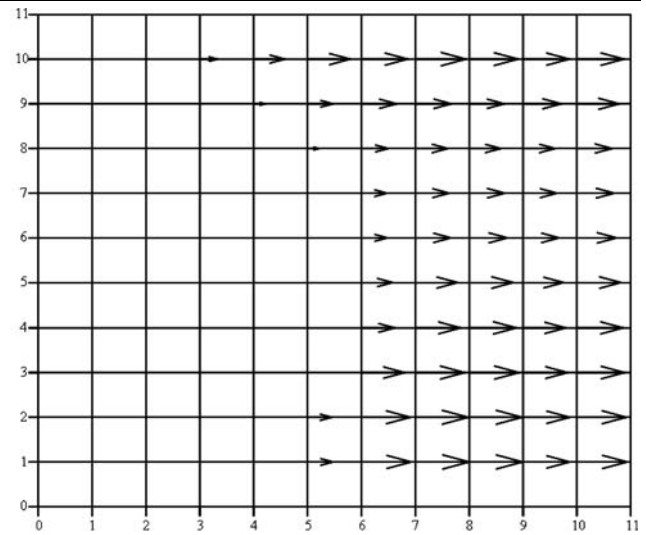
Fig. 18(b). The values of the total frictional dissipation energies calculated in all contact points are given in Table 5.

In the unloading case the tangential forces change sign retaining sign of the total displacements. For smaller friction coefficients the change of sign of the tangential forces corresponds to a greater value of the force at unloading. For the same directional parameters  $\mu$  and  $\nu$  and the same axial compliance parameters the behaviour of the contact surfaces must be symmetric (Figs. 18(a), 18(b), 19(a) and 19(b)). It is not so for other axial parameters (Figs. 18(c) and 19(c)). The values of the plastic displacements are smaller for larger principal friction coefficients. The results obtained for different interface contact parameters and the same principal



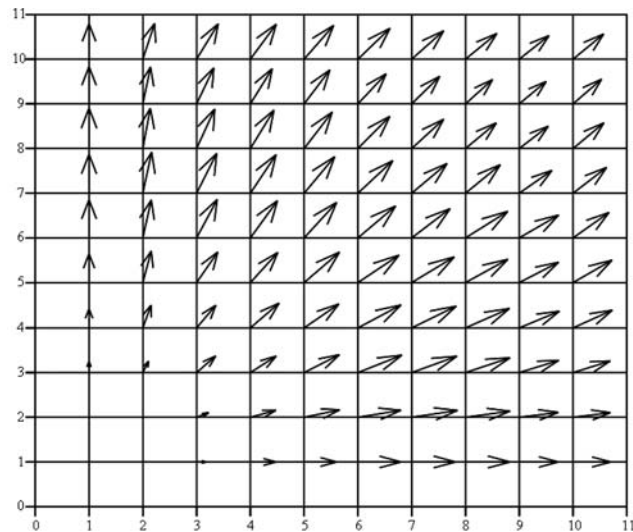
(plastic\_disp\_x,plastic\_disp\_y)

(a)



(plastic\_disp\_x,plastic\_disp\_y)

(c)



(plastic\_disp\_x,plastic\_disp\_y)

(b)

**Fig. 19** Directions of tangential plastic displacements at 100 contact points using 28-node transition elements for different slip models and external load value of 1000 N;  $m_{00} = 0.625$ ,  $m_{20} = 8. \times 10^{-5}$ ,  $m_{02} = 8. \times 10^{-4}$ ,  $m_{40} = 1.04 \times 10^{-6}$ ,  $m_{04} = 1.04 \times 10^{-4}$ ,  $E_1 = E_2 = 2. \times 10^5$  N/mm<sup>2</sup>,  $\nu_1 = \nu_2 = 0.25$ ,  $Y = 2070$  N/mm<sup>2</sup>,  $K = 1.62$ ,  $\psi = 0.35$ ,  $c_h = 0.967\omega_p/\omega_c = 45$ .: (a)  $\mu_{m_x} = \mu_{m_y} = 0.2$ ,  $\mu_{o_x} = \mu_{o_y} = 1.$ ,  $\nu_x = \nu_y = 0.125$ ,  $k_{T_x} = k_{T_y} = 0.7k_n$ , (b)  $\mu_{m_x} = \mu_{m_y} = 0.5$ ,  $\mu_{o_x} = \mu_{o_y} = 0.5$ ,  $\nu_x = \nu_y = 0.125$ ,  $k_{T_x} = k_{T_y} = 0.7k_n$ , (c)  $\mu_{m_x} = \mu_{m_y} = 0.5$ ,  $\mu_{o_x} = \mu_{o_y} = 0.5$ ,  $\nu_x = \nu_y = 0.125$ ,  $k_{T_x} = 0.7k_n$ ,  $k_{T_y} = k_n$

(axial) friction coefficients show that the values of plastic displacements are greater for greater values of the axial contact stiffness.

The general contact behaviour is in qualitative agreement with the results obtained in [83, 85]. The values calculated here cannot be compared with those of [83, 85], because

**Fig. 19** (Continued)

different FEM-meshes and different friction models were taken therein.

### 10 Conclusions

1. A hardening friction model, which is analogous to the incremental theory of plasticity, including both the isotropic and orthotropic properties of the contact interface, has been proposed.
2. Both the elastic and elasto-plastic stiffness coefficients decrease with increasing variance of the surface height about the mean plane,  $m_{00}$ .
3. A detectable difference between the elastic and elasto-plastic normal stiffness for the high normal pressure is observed. The elasto-plastic stiffness increases slowly as the plasticity index  $\psi$  decreases.
4. The standard deviation of slopes and standard deviation of curvatures have no observable effects on the normal stiffness.

**Acknowledgements** Sponsorship of the work by the Ministry of Science and Higher Education under grant numbers N N519 402537 to the Maritime University of Szczecin (R.B.) and N519 01031/1601 to the Institute of Fundamental Technological Research (M.K.) is gratefully acknowledged.

### Appendix A

The elements of the covariance matrix  $N_{ij}$  are computed in the following way.

Assume that the surface height  $z(x, y)$  is represented by infinite sum

$$z(x, y) = \sum_n C_n \cos(xk_{xn} + yk_{yn} + \epsilon_n),$$

where  $k_x$  and  $k_y$  are the components of a wave vector  $\mathbf{k}$  and  $\epsilon_n$  is a random phase with a uniform probability of lying in the range  $(0, 2\pi)$ .

The power spectral density function (PSD)  $\Phi(k_x, k_y)$  is given by the Fourier transform of the autocorrelation function  $R(x, y)$

$$\Phi(k_x, k_y) = \frac{1}{4\pi^2} \int_{-\infty}^{+\infty} \int_{-\infty}^{+\infty} R(x, y) \times \exp[-i(xk_x + yk_y)] dx dy$$

and the inverse relation holds

$$R(x, y) = \int_{-\infty}^{+\infty} \int_{-\infty}^{+\infty} \Phi(k_x, k_y) \times \exp[i(xk_x + yk_y)] dk_x dk_y.$$

In particular case

$$\sigma^2 = R(0, 0) = m_{00} = \int_{-\infty}^{+\infty} \int_{-\infty}^{+\infty} \Phi(k_x, k_y) dk_x dk_y.$$

The statistical moments  $m_{pq}$  are defined by the PSD function  $\Phi(k_x, k_y)$

$$m_{pq} = \int_{-\infty}^{+\infty} \int_{-\infty}^{+\infty} \Phi(k_x, k_y) k_x^p k_y^q dx dy.$$

The coefficients  $C_n$  are related to the PSD function by

$$\frac{1}{2} \sum_{\Delta k} C_n^2 = \Phi(k_x, k_y) dk_x dk_y.$$

We have from above equations

$$m_{pq} = \frac{1}{2} \sum_n k_{xn}^p k_{yn}^q C_n^2.$$

As example of how the elements of matrix  $N_{ij}$  are computed, consider the elements  $n_{14}$  and  $n_{23}$

$$n_{14} = E[\xi_1 \xi_4] = \overline{\xi_1 \xi_4} = - \sum_n C_n^2 k_{xn}^2 \overline{\cos^2(xk_{xn} + yk_{yn} + \epsilon_n)},$$

and if the average on the right-hand side of above equation is taken over  $\epsilon_n$ , we have

$$E[\xi_1 \xi_4] = \overline{\xi_1 \xi_4} = - \frac{1}{2\pi} \int_0^{2\pi} \sum_n C_n^2 k_{xn}^2 \cos^2(xk_{xn} + yk_{yn} + \epsilon_n) d\epsilon_n.$$

The above integral may be evaluated analytically to give

$$n_{14} = E[\xi_1 \xi_4] = \overline{\xi_1 \xi_4} = - \frac{1}{2} \sum_n C_n^2 k_{xn}^2 = -m_{20}.$$

In the case of element  $n_{23}$ , we have

$$n_{23} = E[\xi_2 \xi_3] = \overline{\xi_2 \xi_3} = \sum_n C_n^2 k_{xn} k_{yn} \overline{\sin^2(xk_{xn} + yk_{yn} + \epsilon_n)},$$

and if the average on the right-hand side of above equation is taken over  $\epsilon_n$ , we have

$$E[\xi_2 \xi_3] = \overline{\xi_2 \xi_3} = - \frac{1}{2\pi} \int_0^{2\pi} \sum_n C_n^2 k_{xn} k_{yn} \sin^2(xk_{xn} + yk_{yn} + \epsilon_n) d\epsilon_n$$

and

$$n_{23} = E[\xi_2 \xi_3] = \overline{\xi_2 \xi_3} = \frac{1}{2} \sum_n C_n^2 k_{xn} k_{yn} = m_{11}.$$

Then the covariance matrix  $N_{ij}$  is found to be

$$N_{ij} = \begin{bmatrix} n_{11} & n_{12} & n_{13} & n_{14} & n_{15} & n_{16} \\ n_{21} & n_{22} & n_{23} & n_{24} & n_{25} & n_{26} \\ n_{31} & n_{32} & n_{33} & n_{34} & n_{35} & n_{36} \\ n_{41} & n_{42} & n_{43} & n_{44} & n_{45} & n_{46} \\ n_{51} & n_{52} & n_{53} & n_{54} & n_{55} & n_{56} \\ n_{61} & n_{62} & n_{63} & n_{64} & n_{65} & n_{66} \end{bmatrix} = \begin{bmatrix} m_{00} & 0 & 0 & -m_{20} & -m_{11} & -m_{02} \\ 0 & m_{20} & m_{11} & 0 & 0 & 0 \\ 0 & m_{11} & m_{02} & 0 & 0 & 0 \\ -m_{20} & 0 & 0 & m_{40} & m_{31} & m_{22} \\ -m_{11} & 0 & 0 & m_{31} & m_{22} & m_{13} \\ -m_{02} & 0 & 0 & m_{22} & m_{13} & m_{04} \end{bmatrix}.$$

**References**

1. Greenwood JA, Williamson JBP (1966) Contact of nominally flat surfaces. Proc R Soc Lond A 295:300–319
2. Komvopoulos K, Choi D-H (1992) Elastic finite element analysis of multi-asperity contacts. J Tribol 114:823–831
3. Greenwood JA (1984) A unified theory of surface roughness. Proc R Soc Lond A 393:133–157
4. Fardin N, Stephansson O, Jing L (2001) The scale dependence of rock joint surface roughness. Int J Rock Mech Min Sci 38:659–669
5. Fardin N, Feng Q, Stephansson O (2004) Application of a new in situ 3D laser scanner to study the scale effect on the rock joint surface roughness. Int J Rock Mech Min Sci 41:329–335
6. Whitehouse DJ (2001) Fractal or fiction. Wear 249:345–353
7. Greenwood JA (2002) Comments on ‘Fractal or fiction’ by DJ Whitehouse. Wear 252:842–843

8. Greenwood JA, Wu JJ (2001) Surface roughness and contact: an apology. *Meccanica* 36:617–630
9. Radziejewska J (2005) Determination of 3D roughness parameters in contact problems. *Adv Manuf Sci Technol* 29:5–19
10. Majumdar A, Bhushan B (1990) Role of fractal geometry in roughness characterization and contact mechanics of surfaces. *J Tribol Trans ASME* 112:205–216
11. Sayles RS, Thomas TR (1979) Measurements of the statistical microgeometry of engineering surfaces. *J Lubr Technol Trans ASME* 101:409–418
12. Sayles RS, Thomas TR (1976) Thermal conductance of a rough elastic contact. *Appl Energy* 2:249–267
13. McCool JI (1978) Characterization of surface anisotropy. *Wear* 49:19–31
14. Whitehouse J, Archard JF (1970) The properties of random surfaces in contact. *Proc R Soc Lond A* 316:97–121
15. Nayak PB (1971) Random process model of rough surfaces. *J Lubr Technol Trans ASME* 93:398–407
16. Nayak PB (1973) Some aspects of surface roughness measurement. *Wear* 26:165–174
17. Bush AW, Gibson RD, Thomas TR (1975) The elastic contact of a rough surfaces. *Wear* 35:87–111
18. Bush AW, Gibson RD, Keogh GP (1976) The limit of elastic deformation in the contact of rough surfaces. *Mech Res Commun* 3:169–174
19. Bush AW, Gibson RD, Keogh GP (1979) Strongly anisotropic rough surfaces. *J Lubr Technol Trans ASME* 101:15–20
20. Sayles RS, Thomas TR (1978) Surface topography as nonstationary random process. *Nature* 271:431–434
21. Whitehouse DJ, Phillips MJ (1978) Discrete properties of random surfaces. *Philos Trans R Soc Lond A* 290:267–298
22. Whitehouse DJ, Phillips MJ (1982) Two-dimensional discrete properties of random surfaces. *Philos Trans R Soc Lond A* 305:441–468
23. Whitehouse DJ, Phillips MJ (1985) Sampling in a two-dimensional plane. *J Phys A, Math Gen* 18:2465–2477
24. Pullen J, Williamson JBP (1972) On the plastic contact of rough surfaces. *Proc R Soc Lond A* 327:159–173
25. Chang WR, Etsion I, Bogy DB (1987) An elastic plastic model for the contact of rough surfaces. *J Tribol Trans ASME* 109:257–263
26. Hornig JH (1998) An elliptical elastic-plastic asperity microcontact model for rough surfaces. *J Tribol Trans ASME* 120:82–88
27. Longuet-Higgins MS (1957) The statistical analysis of a random, moving surface. *Philos Trans R Soc Lond A* 249:321–387
28. Longuet-Higgins MS (1957) Statistical properties of an isotropic random surface. *Philos Trans R Soc Lond A* 250:157–174
29. So H, Liu DC (1991) An elastic-plastic model for the contact of anisotropic rough surfaces. *Wear* 146:201–218
30. McCool JI, Gassel SS (1981) The contact of two surfaces having anisotropic roughness geometry. *ASLE Special Publication SP 7*, pp 29–38
31. Kucharski S, Klimczak T, Polijaniuk A, Kaczmarek J (1994) Finite elements model for the contact of rough surfaces. *Wear* 177:1–13
32. Kogut L, Etsion I (2002) Elastic-plastic contact analysis of a sphere and a rigid flat. *J Appl Mech Trans ASME* 69:657–662
33. Larsson J, Biwa S, Storåkers B (1999) Inelastic flattening of rough surfaces. *Mech Mater* 31:29–41
34. Faulkner A, Arnell RD (2002) The development of a finite element model to simulate the sliding interaction between two, three-dimensional, elasto-plastic, hemispherical asperities. *Wear* 242:114–122
35. Lin LP, Lin JF (2007) An elliptical elastic-plastic microcontact model developed for an ellipsoid in contact with a smooth rigid flat. *Wear* 129:772–782
36. Yang J, Komvopoulos K (2005) A mechanics approach to static friction of elastic-plastic fractal surfaces. *J Tribol ASME* 127:315–324
37. Hyun S, Pei L, Molinari J-F, Robbins MO (2004) Finite-element analysis of contact between elastic self-affine surfaces. *Phys Rev E* 70(026117):1–12
38. Pei L, Hyun S, Molinari J-F, Robbins MO (2005) Finite element modeling of elasto-plastic contact between rough surfaces. *J Mech Phys Solids* 53, 2385–2409
39. Wriggers P (1995) Finite element algorithms for contact problems. *Arch Comput Methods Eng* 2:1–49
40. Thomas TR (1999) *Rough surfaces*, 2nd edn. Imperial College Press, London
41. Bhushan B (1990) *Tribology and mechanics of magnetic storage devices*. Springer, New York
42. Bhushan B (1994) Tribology of solid contacts in magnetic recording devices. *Appl Mech Rev ASME* 47:199–203
43. Bhushan B (1998) Contact mechanics of rough surfaces in tribology: multiple asperity contact. *Tribol Lett* 4:1–35
44. Whitehouse DJ (1994) *Handbook of surface metrology*. Institute of Physics Publishing, Bristol
45. Ciavarella M, Murolo G, Demelio G, Barber JR (2004) Elastic contact stiffness and contact resistance for Weierstrass profile. *J Mech Phys Solids* 52:1247–1265
46. Ciavarella M, Delfino V, Demelio G (2006) A re-vitalized Greenwood and Willimason model of elastic contact between fractal surfaces. *J Mech Phys Solids* 54:2569–2591
47. Persson BNJ, Albohr O, Tratagliano U, Volokitin AI, Tosatti E (2005) On the nature of surface roughness with application to contact mechanics, sealing, rubber friction and adhesion. *J Phys, Condens Matter* 17:R1–R62
48. McCool JI (1986) Comparison of models for the contact of rough surfaces. *Wear* 107:37–60
49. Willner K, Gaul L (1997) Contact description by FEM based on interface physics. In: Owen DRJ, Oñate E, Hinton E (eds) *Proc 4th int conf COMPLAS*. Pineridge Press, Swansea, pp 884–891
50. Zavarise G, Schrefler BA (1995) Numerical analysis of microscopically elastic contact problems. In: Raous M, Jean M, Moreau JJ (eds) *Proc 2nd int contact mechanics int symp*. Plenum, New York, pp 305–312
51. Buczkowski R, Kleiber M (1999) A stochastic model of rough surfaces for finite element contact analysis. *Comput Methods Appl Mech Eng* 169:43–59
52. Buczkowski R, Kleiber M (2006) Elasto-plastic statistical model of strongly anisotropic rough surfaces for finite element 3D-contact analysis. *Comput Methods Appl Mech Eng* 195:5141–5161
53. Zhao Y, Maietta DM, Chang L (2000) An asperity microcontact model incorporating the transition from elastic deformation to fully plastic flow. *J Tribol Trans ASME* 122:86–93
54. Jeng Y-R, Wang P-Y (2003) An elliptical microcontact model considering elastic, elastoplastic, and plastic deformation. *J Tribol Trans ASME* 125:232–240
55. Abramowitz M, Stegun IA (1972) *Handbook of mathematical functions with formulas, graphs, and mathematical tables*. Dover, New York
56. Brewe DE, Hamrock BJ (1977) Simplified solution for elliptical-contact deformation between two elastic solids. *J Lubr Technol Trans ASME* 99:485–487
57. A Dyson, Evans HP, Snidle RW (1992) A simple, accurate method for calculation of stresses and deformations in elliptical Hertzian contacts. *Proc Inst Mech Eng Part C, J Mech Eng Sci* 206:139–141
58. Greenwood JA (1997) Analysis of elliptical Hertzian contacts. *Tribol Int* 30:235–237
59. Johnson KL (1985) *Contact mechanics*. Cambridge University Press, Cambridge

60. Jamari J, Schipper DJ (2006) An elastic-plastic contact model of ellipsoid bodies. *Tribol Lett* 21:262–271
61. Wu C, Zheng L (1988) A general expression for plasticity index. *Wear* 121:161–172
62. Tabor D (1951) *The hardness of metal*. Oxford University Press, Oxford
63. Francis HA (1976) Phenomenological analysis of plastic spherical indentation. *J Eng Mater Technol Trans ASME* 76:272–181
64. Kogut L, Etsion I (2002) A finite element based elastic-plastic model for the contact of rough surfaces. *Tribol Trans* 46:383–390
65. Shoukry SN (1980) Some aspects of the dynamic performance of machine tool structural joints. PhD Thesis, University of Aston in Birmingham
66. Buczkowski R, Kleiber M (1997) Elasto-plastic interface model for 3D-frictional orthotropic contact problems. *Int J Numer Methods Eng* 40:599–619
67. Maksak WI (1975) Microsliding and contact stiffness of metallic bodies. *Nauka, Moscow* (in Russian)
68. Felder E (1988) Experimental study of the frictional anisotropy of mild steel sheet. *J Mech Theory Appl* 7:479–504 (in French)
69. Jing L, Stephansson O (1995) Mechanics of rock joints: experimental aspects. In: Selvadurai APS, Boulon MJ (eds) *Mechanics of geomaterial interfaces*. Elsevier, Amsterdam, pp 317–342
70. Huber MT (1949) The friction forces and the part they play in some railway problems. *Arch Mech* 1:271–310 (in Polish)
71. Michałowski R, Mróz Z (1978) Associated and non-associated sliding rules in contact friction problems. *Arch Mech* 30:259–276
72. Zmitrowicz A (1981) A theoretical model of anisotropic dry friction. *Wear* 73:9–39
73. Zmitrowicz A (1989) Mathematical descriptions of anisotropic friction. *Int J Solids Struct* 25:837–862
74. Zmitrowicz A (2006) Models of kinematics dependent anisotropic and heterogenous friction. *Int J Solids Struct* 43:4407–4451
75. Felder E (1986) Friction, adhesion, lubrication. A model of anisotropic solid friction. *C R Acad Sci Paris Ser II* 303:643–646 (1986) (in French)
76. Ho Q-C, Curnier A (1993) Anisotropic dry friction between two orthotropic surfaces undergoing large displacements. *Eur J Mech A/Solids* 12:631–666
77. Hohberg J-H (1992) A joint element for the nonlinear dynamic analysis of arch dams. Birkhäuser, Basel
78. Mróz Z, Stupkiewicz S (1994) An anisotropic friction and wear model. *Int J Solids Struct* 31:1113–1131
79. Konyukhov A, Schweizerhof K (2006) Covariant description for frictional contact problems. *Comput Mech* 35:190–213
80. Konyukhov A, Schweizerhof K (2006) Formulation and analysis of the computational model, Part 1. *Comput Methods Appl Mech Eng* 196:103–117
81. Konyukhov A, Vielsack P, Schweizerhof K (2008) On coupled models of anisotropic contact surfaces and their experimental validation. *Wear* 264:579–588
82. Hjjaj M, Feng Z-Q, de Saxce G, Mróz Z (2004) On the modelling of complex anisotropic frictional contact laws. *Int J Eng Sci* 42:1013–1034
83. Klarbring A (1985) A mathematical programming approach to three-dimensional contact problems. *Comput Methods Appl Mech Eng* 58:175–200
84. Alart P (1992) A simple contact algorithm in applied to large sliding and anisotropic friction. In: Curnier A (ed) *Proc contact mechanics intern symp*, October 7–9, EPLF, Lausanne, Switzerland, pp 321–336
85. Park JK, Kwak BM (1994) Three-dimensional frictional contact analysis using the homotopy method. *J Appl Mech ASME* 61:703–709
86. Barbero EJ, Luciano R, Sacco E (1995) Three-dimensional plate and contact/friction elements for laminated composite joints. *Comput Struct* 54:689–703
87. Jones RE, Papadopoulos P (2006) Simulating anisotropic frictional response using smoothly interpolated traction fields. *Comput Methods Appl Mech Eng* 195:588–613
88. Konyukhov A, Schweizerhof K (2006) Formulation and analysis of the computational model, Part 2. *Comput Methods Appl Mech Eng* 196:289–303
89. Jing J, Nordlund E, Sthepansson OA (1994) 3-D constitutive model for rock joints with anisotropic friction and stress dependency in shear stiffness. *Int J Rock Mech Min Sci Geomech Abstr* 31:173–178
90. Fredriksson B (1975) Experimental determination frictional properties in araldite b contacts. Rep LiTH-IKP-R-061, Linköping Institute of Technology
91. Mindlin RD (1949) Compliance of elastic bodies in contact. *J Appl Mech ASME* 71:259–268
92. Selvadurai APS, Au MC (1987) Non-linear interactions in flat anchors embedded in geological media. In: Desai CS et al (eds) *Constitutive laws for engineering materials. Theory and applications*, vol II. Elsevier, New York, pp 1093–1107
93. Habraken A-M, Radu JP, Charlier R (1992). Numerical approach of contact with friction between two bodies in large deformations. In: Curnier A (ed) *Proc contact mechanics int symp PPUR Lausanne*, pp 391–408
94. Plesha ME (1995) Rock joints: theory, constitutive equations. In: Selvadurai APS, Boulon MJ (eds) *Mechanics of geomaterial interfaces*. Elsevier, Amsterdam, pp 375–393
95. Vermeer PA, de Borst R (1984) Non-associated plasticity for soils, concrete and rock. *Heron* 29(3)
96. Black AJ, Kopalinsky EM, Oxley PLB (1993) Asperity deformation models for explaining the mechanisms involved in metallic sliding friction and wear—a review. *Proc Inst Mech Eng, Part C, J Mech Eng Sci* 207:335–353
97. Mróz Z, Stupkiewicz S (1998) Constitutive model of adhesive and ploughing friction in metal-forming processes. *Int J Mech Sci* 40:281–303
98. Buczkowski R, Gabbert U (2004) 28-noded hexahedral isoparametric element for analysis of contact problems. *Commun Numer Methods Eng* 20:147–161
99. Buczkowski R (1998) 21-noded hexahedral isoparametric element for analysis of contact problems. *Commun Numer Methods Eng* 14:681–692
100. Klarbring A (1986) The influence of slip hardening and interface compliance on contact stress distributions. A mathematical programming approach. In: Selvadurai APS, Voyiadjis GZ (eds) *Mechanics of material interfaces*. Elsevier, Amsterdam, pp 43–59